

A new methodology to train fracture network simulation using Multiple Point Statistics

Pierre-Olivier BRUNA^{(1)*}, Julien STRAUBHAAR⁽²⁾, Rahul PRABHAKARAN^(1, 3), Giovanni BERTOTTI⁽¹⁾, Kevin BISDOM⁽⁴⁾, Grégoire MARIETHOZ⁽⁵⁾, Marco MEDA⁽⁶⁾.

(1) Department of Geoscience and Engineering, Delft University of Technology, Delft, the Netherlands.

(2) Centre d'hydrogéologie et de géothermie (CHYN), Université de Neuchâtel, Emile-Argand 11, CH-2000 Neuchâtel.

(3) Department of Mechanical Engineering, Section of Energy Technology, Eindhoven University of Technology, Eindhoven the Netherlands.

(4) Shell Global Solutions International B.V., Grasweg 31, 1031HW Amsterdam, The Netherlands

(5) University of Lausanne, Institute of Earth Surface Dynamics (IDYST) UNIL-Mouline, Geopolis, office 3337, 1015 Lausanne, Switzerland

(6) ENI Spa, Upstream and Technical Services, San Donato Milanese, Italy.

* Corresponding author, p.b.r.bruna@tudelft.nl

Keywords: geostatistics, multiple training images, probability map, fracture networks, stress-induced fracture aperture, outcrop.

Abstract

Natural fracture network characteristics can be known from high-resolution outcrop images acquired from drone and photogrammetry. Such images might also be good analogues of subsurface naturally fractured reservoirs and can be used to make predictions of the fracture geometry and efficiency at depth. However, even when supplementing fractured reservoir models with outcrop data, gaps in that model will remain and fracture network extrapolation methods are required. In this paper we used fracture networks interpreted in two outcrops from the Apodi area in Brazil to present a revised and innovative method of fracture network geometry prediction using the Multiple Point Statistics (MPS) method.

The MPS method presented in this article uses a series of small synthetic training images (TIs) representing the geological variability of fracture parameters observed locally in the field. The TIs contain the statistical characteristics of the network (i.e. orientation, spacing, length/height and topology) and allow representing complex arrangement of fracture networks. These images are flexible as they can be simply sketched by the user. We proposed to use simultaneously a set of training images in specific elementary zones of the Apodi outcrops in order to best replicate the non-stationarity of the reference network. A sensitivity analysis was conducted to emphasize the influence of the conditioning data, the simulation parameters and the used training images. Fracture density computations were performed on selected realisations and compared to the reference outcrop fracture interpretation to qualitatively evaluate the accuracy of our simulations. The method proposed here is adaptable in terms of training images and probability map to ensure the geological complexity is accounted for in the simulation process. It can be used on any type of rock containing natural fractures in any kind of tectonic context. This workflow can also be applied to the subsurface to predict the fracture arrangement and fluid flow efficiency in water, geothermal or hydrocarbon fractured reservoirs.

I] Introduction

I.1 The importance of the prediction of fracture network geometry

Fractures are widespread in Nature and depending on their density and their aperture, they might have a strong impact on fluid flow and fluid aquifers (Berkowitz, 2002; Rzonca, 2008), and in geothermal (Montanari et al., 2017; Wang et al., 2016) and hydrocarbon reservoirs (Agar and Geiger, 2015; Lamarche et al., 2017; Solano et al., 2010) They are typically organised as networks ranging from nanometre to multi-kilometre scale (Zhang, 2016), and present systematic geometrical characteristics (i.e. type, orientation, size, topology) that are

determined from specific stress and strain conditions. These conditions have been used to derive concepts of fracture arrangements in various tectonic contexts and introduced the notion of geological fracture-drivers (fault, fold, burial, facies). Based on these drivers it is possible to some extent to predict reservoir heterogeneity and to define potential permeability pathways within the rock mass (Lamarche et al., 2017; Laubach et al., 2018). Despite the existence of these concepts, a range of parameters including fracture abutment relationships as well as height/length distributions cannot be adequately sampled along a 1D borehole and are mainly invisible on seismic images. In addition, fracture networks may present a spatial complexity (variability of orientation or clustering effect) that is also largely unknown in the subsurface. Long and Witherspoon, (1985) and Olson et al., (2009) showed how those parameters impact the connectivity of the network and consequently affect fluid flow in the subsurface. In outcrops, the fracture network characteristics can be observed in 2D and understood directly. Consequently, outcrops are essential to characterize fracture network attributes that cannot be sampled in the subsurface, such as length or spatial connectivity.

I.2 Surface rocks as multiscale reservoir analogues

In this context, the study of outcrop analogues is one of the few ways to constrain the architecture of fracture networks (Bisdom et al., 2014; Bruna et al., 2017; National Research Council, 1996; Lamarche et al., 2012; Lavenu et al., 2013). Outcrops can be considered as a natural laboratory where the structural reality can be observed and quantified at various scales. At the small – measurement station – scale (order of 10's m), fracture type, chronologies and topology relationships can be characterised using classical ground-based structural geology method such as scanlines (Lavenu et al., 2013; Mauldon et al., 2001). At the intermediate – outcrop – scale (order of 10²'s m), length of fractures and geometry variability can be qualified and quantified using unmanned aerial vehicles (UAV - drones).

Working on outcrops allows an understanding of the geological history of the targeted area and possibly to decipher how, when and where fractures were developed. In addition, outcrops constitute an efficient experimental laboratory where some of properties of the fracture network (i.e. fracture distribution, apertures, permeability and fluid flow behaviour) can be known and modelled (Bisdom et al., 2017). At the large – reservoir – scale (order of 10^3 – 10^4 m) satellite imagery and geophysical maps provide the characterisation of the 100's of meter long objects such as large fracture systems or faults.

However, not every outcrop can be considered as a good analogue for the subsurface. Li et al., (2018), in their work on the Upper Cretaceous Frontier Formation reservoir, USA, observed significant differences in the fracture network arrangement in subsurface cores compared to an apparent good surface analogue of the studied reservoir. In the subsurface, fractures appeared more clustered than in the outcrop where the arrangement is undistinguishable from random. The origin of these differences is still debated but these authors suggest that alteration (diagenesis) or local change in pressure-temperature conditions, may have contributed to the observed variability. The near-surface alteration processes (exhumation, weathering) may also contribute to misinterpretations of the characteristics of the network. In this case, one should be particularly careful while using observed networks to make geometry or efficiency (porosity, permeability) predictions in the subsurface. Therefore, the application to the subsurface of the characteristics observed in the outcrop is not always straightforward or even possible, and may lead to erroneous interpretations. Relatively unbiased signals such as stylolites or veins and particular geometric patterns build trust that the studied outcrop can be compared to the subsurface.

I.3 Modelling approaches classically used to model fracture network geometries

The widely used discrete fracture network (DFN) stochastic modelling tools provide statistical representation of fracture networks constrained generally by univariate and random distribution of orientation, size, spacing and density/intensity data (Bisdom et al., 2014; Bisdom et al., 2017; Huang et al., 2017; Panza et al., 2018). The generated models follow a local stationarity hypothesis. This implies that the statistics used during the simulation are constant in the defined area of interest (Deutsch and Journel, 1997; Gringarten and Deutsch, 1999; Gringarten and Deutsch, 2001; Journel and Zhang, 2006). Liu et al., (2009), highlighted the implicit randomisation that conventional DFN models produce and demonstrated that parameters like fracture connectivity are poorly considered in these representations. In addition, it is generally admitted that discrete realisations of thousands of fracture objects at the kilometre scale are computationally very demanding and often even impossible (Jung et al., 2013). Some authors attempted to use a pixel-based method to try to predict fracture network geometries. Bruna et al., (2015), used a dense hydrogeological borehole survey sampling a Lower Cretaceous aquifer in the SE of France to define fracture facies and to model their distribution with two-points geostatistics. In this case, the amount of available data and their consistency helped to provide realistic results. However, far from conditioning data (i.e. boreholes) the fractures simulation are poorly constrained.

The work of Hanke et al., (2018) uses a directional semi-variogram to quantify fracture intensity variability and intersection density. This contribution provides an interesting way to evaluate the outputs of classical DFN approaches but requires a large quantity of input data that are not always available in the subsurface. To represent the fracture network geometry in various geological contexts, an alternative method has to be developed. This innovative method needs to i) explicitly predict the organisation and the characteristics of multiscale fracture objects, ii) take into consideration the spatial variability of the network and iii) require a limited amount of data to be realised.

129

130 **I.4 Multi-point statistics as an alternative to classic DFN approaches**

131 Since Liu et al., (2002), few authors highlighted the potential of using multi-point statistics
132 (MPS) to generate realistic fracture networks (Chugunova et al., 2017; Karimpouli et al.,
133 2017). Strebelle, (2002) showed how the MPS are able to reproduce any type of geological
134 heterogeneities of any shape at any size as long as they present a repetitive character. This
135 characteristic seems particularly well adapted to predict the geometry of a fracture network.
136 The MPS method uses training images (TI) to integrate conceptual geological knowledge into
137 geostatistical simulations (Mariethoz, 2009). The TI is a grid containing geological patterns
138 that are representative of a certain type of geological structure, type and arrangement. The TI
139 can be considered as a synthetic model of the geological heterogeneity (i.e. all the elements
140 characterising a geological object) likely to occur in a larger domain (i.e. reservoir, aquifer,
141 outcrop). The TI must contain the range of geobodies that are intended to be modelled, as well
142 as the relationship these geobodies have with each other (Mariethoz, 2009; Strebelle, 2002).

143

144 **I.5 Objectives and contents of this research**

145 In this paper we propose a MPS workflow considering the geological variability of the
146 fracture network geometry in outcrops (size order of 100m) and a methodology on how to use
147 this method at the reservoir scale. The approach is based on the direct sampling method
148 (Mariethoz et al., 2010) and uses multiple TIs for a single realisation (Wu et al., 2008). The
149 concept of the probability map has been revised here to define where a training image should
150 be used in the simulation grid. Our outcrop-based simulations also take into account “seismic-
151 scale” objects (i.e. object longer than 40m) considered as hard conditioning data. The
152 proposed workflow is tested on outcrops where fracture network have been previously
153 characterised and interpreted from drone imagery. The studied outcrops are considered as

analogues of the Potiguar Basin, Brazil (Bertotti et al., 2017; Bisdom, 2016). Uncertainties were evaluated by comparing original outcrop interpretation (done manually by a geologist) with the geometrical characteristics of the network generated from MPS. To evaluate the quality of the simulations, we computed density maps in outcrop fracture interpretation and on selected stochastic models. The proposed approach is innovative and provides a quick and efficient way to represent fracture network arrangements at various scales.

II] Methodology

II.1 The direct sampling method

The direct sampling method (DS) was introduced by Mariethoz et al., (2010). Figure 1, synthesizes the DS modelling process developed thereafter. The method requires a simulation grid where each node is initially unknown and called \mathbf{x} , a training image grid (TI) where each node is known and called \mathbf{y} i.e. $V(\mathbf{y})$ is defined where V is the variable of interest (e.g. facies value). The simulation proceeds as follows. First, the set of conditioning data (if present) is integrated in the simulation grid. Then, each remaining unknown node \mathbf{x} is visited following a random or defined path, and simulated as follows. 1) The pattern $\mathbf{d}_n(\mathbf{x}) = (\mathbf{x}_1, V(\mathbf{x}_1)), \dots, (\mathbf{x}_n, V(\mathbf{x}_n))$ formed by the at most \mathbf{n} informed nodes the closest to \mathbf{x} is retrieved. Any neighbour \mathbf{x}_i of \mathbf{x} is either a previously simulated node or comes from the conditioning data set. The lag vectors $\mathbf{h}_i = \mathbf{x}_i - \mathbf{x}$ define the geometry of the neighbourhood of \mathbf{x} . The combination of the value and position of \mathbf{x}_i defines the data event or pattern $\mathbf{d}_n(\mathbf{x})$. 2) Then, the TI is randomly scanned to search for a pattern $\mathbf{d}_n(\mathbf{y})$ similar to $\mathbf{d}_n(\mathbf{x})$. For each scan node \mathbf{y} , the pattern $\mathbf{d}_n(\mathbf{y}) = (\mathbf{y}_1, V(\mathbf{y}_1)), \dots, (\mathbf{y}_n, V(\mathbf{y}_n))$, where $\mathbf{y}_i = \mathbf{y} + \mathbf{h}_i$, is compared to $\mathbf{d}_n(\mathbf{x})$ using a distance (Meerschman et al., 2013). When the distance is lower than an acceptance threshold (t) defined by the user or if the proportion of scanned nodes in the TI reaches a maximal fraction

(**f**) defined by the user, the scan is stopped and the value of the best candidate y (pattern with the minimal distance) is directly attributed to x in the simulation grid (i.e. $V(x) = V(y)$).

As the DS method does not use a catalogue of all possible patterns found in the TI, it is extremely flexible and in particular allows taking into account both categorical and continuous variables and managing multivariate cases, provided that the pattern distance is suitable. In this paper we are using the DeeSse version of the direct sampling code (Straubhaar, 2017).

II.2 Multiscale fracture attributes

To evaluate how the direct sampling method deals with the fracture network, the present experimentation is based on outcrop data where the present-day structural reality is observable at various scales. Pavements (i.e. horizontal surfaces in the order of 10^2 m scale) were targeted because they contain important information that is not always accessible with vertical outcrops (Corradetti et al., 2017a; Corradetti et al., 2017b; Tavani et al., 2016) or with geophysical imagery (e.g. seismic data). The size of pavements allow the user to interpret a large amount of fracture and to define areas where the geometry of the network varies (Bruna et al., 2018). Pavements also allow to obtain quantitative data on fracture lengths, which are usually difficult to get in vertical cliff. In the subsurface, data can be provided by geophysical 3D maps and fracture attribute detection tools (Chopra and Marfurt, 2007; Somasundaram et al., 2017). However, these tools are not always available and detect the longer lineaments only.

Working with pavements constitutes an asset as small-scale investigation can be conducted in key zones of the outcrop (i.e. in folded areas, each compartment or dip domain of the fold should be imaged and investigated in detail where the gathered data will help to calibrate larger scale information. Classical fieldwork methods (observation and characterisation,

measurements, statistical analyses, sampling) help interpreting fracture families and are essential to constrain larger scale observation.

In this study, UAV-based photogrammetry is used to obtain an orthorectified mosaic and 3D digital outcrops models (Bemis et al., 2014; Claes et al., 2017; Vollgger and Cruden, 2016). The scale of these images is an intermediate between the scale of measurement station and that of satellite imagery. Digitization of fracture traces, geological contacts, sedimentary structures and structural domain boundaries are currently processed by hand and represent a considerable time investment. In this contribution, fractures were interpreted in orthomosaic images with the help of GIS software. Length, azimuth, fracture family proportions and fracture density statistics were extracted from the interpretation. In addition, a series of measurement station (area of about 2×2 m) information was acquired and compared with the dataset from the drone imagery in order to align interpretations and provide coherent fracture history.

II.3 Training images, conditioning data and probability maps

• Training images

Training images (TI) are the base input data of the MPS simulation. Building them is a critical step to succeed a realisation (Liu et al., 2009). The TI is a pixelated image based on a local interpretation of a geological phenomenon (i.e. an interpreted photography taken from a local zone of interest in the field) or digitised by a geologist and based on geological concepts (Strebelle, 2002). As the MPS algorithms borrow patterns from the TIs to populate the simulation grid, one should use TIs synthesising all of the recognized geological parameters that characterise the area to simulate. To model non-stationary fields, i.e. fields where the characteristics of the patterns differ depending on their location, one can follow two strategies. The first one consists in using a non-stationary TI containing all wanted spatial

features. This requires to build one or several auxiliary variables describing the non-stationarity in the TI and to define these auxiliary variables in the simulation grid to constrain the simulation and indicate which kind of patterns will be simulated in which locations (Chugunova and Hu, 2008; Mariethoz et al., 2010; Straubhaar et al., 2011). The second approach consists in using several stationary TIs, each one depicting the same kind of patterns everywhere, and defining zones in the simulation grid corresponding to each specific TI. This second approach is chosen in this work, because it allows to define simple geological concepts (TIs) specific to regions delineated in the simulation domain. The facies proportions and their spatial arrangement belongs to each TI and can vary from one image to the other (figures 5, 6, 9 and 10). Each TI has a local impact on the simulation. Moreover, in our approach fractures sets are grouped in facies in the TI, based primarily on their orientation and possibly on their length or additional parameters defined by the user. The fractures classification helps reproducing patterns and simplifies the process of building the TIs. Note also that two TIs used for two adjacent zones should share some common features in order to obtain realistic transitions between the regions in the simulation domain.

• **Conditioning data**

One limitation of the MPS methods is the tendency to disconnect long continuous objects (i.e. typically fractures, Bruna et al., 2017). To manage this issue, long fractures can be identified and incorporated into the simulation as conditioning data. As per the training images, such data can be integrated as pixelated grids. They may come from satellite imagery or they can be interpreted from gravity or magnetic surveys or from 3D seismic imagery (Magistrini et al., 2014).

• **Probability map**

The direct sampling method can be used with multiple training images. In this situation, the user provides a set of TIs, and for each TI a probability map is defined on the simulation grid,

giving at each node the probability to use that TI. The pixel-wise sum of these maps should then be equal to one in every node. If each TI corresponds to a partition of the area of interest, with for each TI one elementary zone, covering the whole simulation grid, the probabilities in the map are set to one for specific TI and to zero for the other ones.

As per the training images, the probability map comes from a simple sketch (i.e. a pixelated image) given by the MPS user. It is based on the geological concepts or interpretations that define the geometry variability over the simulated area and that allow a partition of the outcrop. In each of the zones defined in the area of interest, the simulated property will follow the intrinsic stationarity hypothesis (Gringarten and Deutsch, 2001; Journel and Zhang, 2006; Journel, 2005) but the entire domain will be non-stationary.

While working on outcrops, the partition of the area of interest can be decided based on observations. For instance, when the fracture network interpreted from outcrop images is available, the geologist can visually define where the characteristics of the network are changing (fracture orientation, intensity, length, topology) and draw limits around zones where the network remains the same (internal variability, Hooker and Katz, 2015). However, in other cases outcrops or subsurface observation could be discontinuous between observation sites. If the data are sparse and come mainly from fieldwork ground observations or boreholes, the use of alternative statistical approaches can help to provide a robust and accurate partition of the area of interest. The work of Marrett et al., (2018) interprets the spatial organisation of fractures using advanced statistical techniques such as normalized correlation count and weighted correlations count, on scanlines collected in the Pennsylvanian Marble Falls Limestone. In their approach, the periodicity of fracture spacing (clustering) calculated from the mentioned techniques is evaluated using Monte Carlo to quantify how different the fracture networks are from a random organisation. These approaches can be highly valuable during the process of building a probability maps when less data are

available. The probability maps provide a large-scale framework that may be refined and modified with additional data such as measurement stations or drone surveys coming from surface exploration or wells data containing fracture network information.

II.4 Testing the simulated network: from pixels to segments

MPS realisations are produced as pixelated images. To evaluate the resulting fracture network, pixels alignments corresponding to fractures are extracted as discrete straight-line objects defined by start and end points. Fractures are separated from the background and in different sets by automatic image classification methods. On grayscale images, this is obtained by multilevel image thresholding through the Otsu's method (Otsu, 1979). On color images, fracture sets are classified based on their color components with the k-means clustering algorithm built in MATLAB (Lloyd, 1982). Image classification gives in output a series of binary images, one for each fracture set, where lineaments are represented as foreground (Kovesi, 2000).

III] Results: test case on analogues of the Potiguar Basin, E Brazil

III.1 Geological setting

The Potiguar Basin is a rift basin located in the easternmost part of the Equatorial Atlantic continental margin, NE Brazil (fig. 2). The basin is found both onshore and offshore (fig. 2). The basin was generated after the initiation of the South American and African breakup during the Jurassic - Early Cretaceous times. It was structured by a first NW-SE extension stage latterly rotating to an E-W extensional direction (Costa de Melo et al., 2016). The rift basin displays an architecture of horsts and grabens striking NE-SW and bounded towards the east and south by major fault systems (de Brito Neves et al., 1984), fig. 2). The Potiguar Basin displays three sedimentary sequences deposited since the Early Cretaceous (i.e. syn- and post

rift depositions). The last post-rift sequence was deposited since the Albian and encompasses the Cenomanian-Turonian Jandaíra Formation. This formation consists of up to 700 m thick bioclastic calcarenites and calcilutites deposited in transgressive shallow marine environment. From the Campanian to the Miocene, the compressive principal stress was oriented N-S (Bertotti et al., 2017). From the Miocene to the Quaternary the onshore part of the Potiguar basin was uplifted. Synchronously, a new compressive stress field was established trending to a NW-SE direction (Reis et al., 2013).

III.2 Outcrop data

The area of interest measures 2.1×1.3 km and is located about 25 km NE of the city of Apodi in the Rio Grande Do Norte state (fig. 2). It contains two outcrops AP3 and AP4 (Bertotti et al., 2017; Bisdom, 2016, fig. 2) here defined respectively as 600×300 m and 400×500 m large pavements localized in the Jandaíra Formation. AP3 and AP4 crop out as pavements with no significant incision. The outcrops are sparsely covered by vegetation and consequently they present a clear fracture network highlighted by karstification. In 2013, images of AP3 and AP4 were acquired using a drone (Bisdom, 2016) and processed using the photogrammetry method. Two high-resolution ortho-rectified images of these pavements (centimetre-scale resolution) were used to complete fracture network interpretation and to extract fracture parameters. In AP3, 775 lineaments were traced (fig. 3) and in AP4, 2593 (fig. 4). These lineaments collectively termed fractures in this paper. For each of these outcrops three fractures sets were identified: set1 striking N135-N165, set2 striking N000-N010/N170-N180 and set 3 striking N075-N105. Fractures falling outside of these ranges were not considered in the input data. Consequently, in AP3 we considered 562 only (out of 775 fractures traced in the pavement) and in AP4 we considered 1810 only out of 2593 fractures. In addition, ground-based fieldwork was conducted in AP3 and AP4 to understand the

structural history of the area and to calibrate the interpretation conducted on the drone aerial photography. General location and fracture data are presented in figure 3 and 4 and in table 1. In AP3, sets 1 and 2 are distributed over the pavement. However, their intensity is variable in the area of interest. Set 3 is mainly expressed in distinct regions of the outcrop. Small-scale investigations (conducted on measurement stations in the outcrop) showed that set 3 is composed of stylolites and sets 1 and 2 of veins. In addition, sets 1 and 2 present evidences of shear movements and are then considered as a conjugate system. In AP4 small-scale investigations highlight the same characteristics as the ones observed in AP3. Although the conjugate system (set 1 and set 2) is less developed there than in AP3. It is also notable that more crosscutting relationships were observed in AP4 compared to AP3.

III.3 Input data for MPS simulation

To evaluate the effect of conditioning data, results of two simulations were compared, with and without conditioning data. The sensitivity of simulation parameters was investigated by varying i) the number of neighbours defining patterns (data events d_n), ii) the acceptance threshold (t) defining the tolerance the algorithm authorises to find a matching data event in the simulation grid (Mariethoz et al., 2010) and iii) the fraction of the TI to be scanned during the simulation process to search for data events. Results of this sensitivity analysis help to propose the best possible simulation for AP3 and to optimise the choice of input parameters for AP4 fracture simulation.

AP3 presents intrinsic fracture network geometry variability. This observation emphasizes that averaging fracture parameters on the entire domain is not well suited to represent the complexity of the network. We observed that the length of fracture per sets and the density of fractures are parameters that vary the most here. The analysis of these variations allow to partition AP3 and AP4 in elementary zones and to synthesize the fracture network

characteristics in each of these domains. The following section defines how the TI, probability map and conditioning data were built.

- **Partitioning, training images and probability map for AP3 and AP4**

We divided AP3 in 5 elementary zones (EZ) based on visual inspection of the pavement (fig. 5A-B). The number of fractures per EZ is synthesized in figure 5. The proportion of fracture per elementary zone is available in table 1. A limited part of the fractures belongs to two adjacent elementary zones. This issue is quantified in table 1.

A probability map with sharp boundaries (fig. 5B) was created for AP3. Sharp boundaries are justified by the variability of the network geometry, which is known from the visual inspection of the interpreted image. Smooth transitions could also be defined (see discussion). The input data to build the probability map is an image of the partition of the area of interest containing the different outcrops. In this image, the indexed zones (elementary zones EZ) are characterised by a distinctive colour.

At the scale of a reservoir where some outcrops analogues and fracture tracing may be available, the interpreted reality of the network (e.g. a binary fracture/non-fracture image) can be directly used as a training image. We chose to ignore the tracing and to rely on parameters that are attained through field observation without having access to drone images of an entire outcrop (i.e. orientation, spacing, abutment) and to compare the interpretation with the simulated network. In that respect fracture orientation were averaged to a single value. Hence, set 1 strikes N090, set 2 strikes N150 and set 3 strikes N180. According to the outcrop partitioning, five training images were created (fig. 5C). In each training image, three facies corresponding to the three fracture sets were created. Set1 is green, set 2 is red and set 3 is blue (fig. 5C). The topology is a crucial problem in fracture simulations because it influences the connectivity of the network. In the MPS simulations the abutments are particularly well reproduced as they represent singular pixels arrangements that are efficiently taken into

account. However, crosscutting relationships imply the use of a different facies at the intersection locus. This method respects and reproduces intersections during the simulation process. In AP3, the analysis of the topology relationships showed three main crosscutting interactions:

- Long fractures from Set 2 and Long fractures from Set 3 mutually crosscut (conjugated sets)
- Set 3 crosscut Set 1
- Set 2 crosscut Set 1

To take into account these topological parameters a different facies colour was attributed to the crosscutting locus (the crossing facies, fig. 6). When the MPS realization will be later discretized, the younger fractures will be truly represented as continuous segments. The older fractures will be cut in pieces but their alignment will be, in most of the case, maintained during the simulation process.

• Dimensions of the simulation grids and of the training images

The dimensions of the simulation grid for AP3 and of each training image (in pixels) are shown in fig.5. The number of pixels is automatically determined by the size of the original drawing made by the geologist.

The size of the input training image does not generally influence the simulation. However, it has to be chosen sufficiently large with respect to the complexity of the patterns in order to get reliable spatial statistics. The DS method tends to identify patterns (i.e. d_n 's see above) in the TI and to paste the central node of them into the simulation grid. However, at a constant resolution and specifically for fractures patterns, it is likely that a 50×50 m training image will carry more complexity and variability than a 10×10 m one. This parameter should be taken into consideration when starting digitizing training images, especially when spacing between fractures is not consistent across the simulation grid.

• Long fractures conditioning

Because the MPS method has the tendency to cut long individual segments into smaller pieces, the fractures longer than 40 meters – the ones visible from satellite/drone imagery in AP3 – were isolated and considered as hard conditioning data (fig. 5D). This threshold was arbitrarily determined from the dataset we have. In AP3, less than 8% of the fractures are longer than 40 m.

In AP3, long fractures belong only to the sets oriented/striking N180 or N150 (fig. 5D). 18 N180 fractures (3% of the whole) and 30 N150 fractures (5% of the whole) were digitized and integrated as conditioning data in the simulation.

III.4 Outcrop scale simulations

III.4.1 Impact of conditioning data on AP3 simulations

In AP3, the 48 long fractures were manually digitized and imported into the simulation grid as categorical properties to be considered as hard conditioning data during the MPS simulation process. The MPS simulation is consequently in charge of stochastically populating the smaller fractures within the grid.

Results of the influence of these data are presented in figure 7. The principal simulation parameters in the considered scenarios (with and without conditioning data) were set up identical (constant acceptance threshold (5%), constant percentage of scanned TI (25%) and constant number of neighbours (50)).

Results showed that the realisation without conditioning data creates 20% less number of fractures than the original outcrop reference. The simulation with conditioning data creates 9% less number of fractures than AP3, which allow to better replicate the long fracture than a non-conditioned simulation. It is also remarkable that the non-constrained simulation represents only 23 fractures above 40 meters (compared to the 48 long fractures interpreted on

the AP3 outcrop). In this simulation the long fractures are essentially located in the zone 3 of the outcrop. Because the simulation is a stochastic process, the location of the long fractures is randomly determined in the absence of hard conditioning data. Considering hard-conditioning data also gives a more realistic representation of the fracture network.

III.4.2 Sensitivity analysis on the AP3 simulation parameters

- **Simulation parameter set-ups, duration and analyses conducted on the results**

Simulation parameters were varied for each simulation in order to emphasize their effect on each realisation. One realisation per test was performed during this analysis. The goal of this analysis is to show how the different parameters influence the reproduction of fracture segments and not to evaluate how good is the matching between the simulation and the reference.

The MPS realisations are pixelated images. The sensitivity analysis is based on the discrete segments extracted from these pixelated images (see II.4). All of the simulations present a variable percentage of segment lengths that are below the minimal fracture length interpreted in the AP3 outcrop (i.e. simulation noise). Consequently all segments smaller than 2.2m were removed from the simulation results. A length frequency distribution was compiled for each of the generated simulations.

The influence of the number of neighbours was evaluated through 7 simulations (SIM1 to SIM7). The acceptance threshold and the number of neighbours was investigated by comparing 8 simulations (SIM8 to SIM15) where the scanned fraction of the TI was fixed at 25%. The percentage of the scanned fraction of the TI was combined with the two other simulation parameters. This combination was tested over 12 simulations (SIM16 to SIM27). The models set-ups and the duration of the simulations are presented in (table 2). It is notable that SIM8 / SIM9, SIM10 / SIM11 and SIM13 / SIM14 produce exactly the same network

despite the modification of the simulation parameters. Also The MPS algorithm successfully performed SIM16 but the segment extraction generated an error preventing the discretisation of all of the objects.

The total amount of generated fractures segments was counted and compared with the total amount of fracture traces interpreted from the original outcrop. A deviation of 10% compared to the original amount of interpreted fractures is considered as a satisfactory result as it is very close to the reference amount of fractures. A deviation of 20% compared to the original amount of interpreted fractures is considered as an acceptable result. This deviation is consequent but can be adjusted by varying the simulation parameters. A deviation above 20% was rejected as a complete reconsideration of the parameters is required. Results are synthesized in table 3.

The total amount of segments was initially counted in the entire simulation domain. The sum of segments per part is constantly higher than the initial total amount of segments because segments cutting a sharp boundary are divided in two - segments falling within two elementary zones and are consequently counted twice. The number of generated fractures per simulation zone was also computed and the same deviation thresholds were applied to evaluate if the simulation is satisfactory, acceptable or rejected. Tables 4 to 6 synthesize the sensitivity analysis conducted of 27 realisations of the AP3 outcrop.

The length of the segments have been computed for each realisation and are presented in figure 8.

The influence of the hard conditioning data and of the drawing of the training image was also quantitatively investigated and compared respectively with the length of the generated segments and with the amount of segments generated per zone.

- **Summary of the results**

Increasing the number of neighbours lengthens the computation time (table 2, SIM 1 to 7). A small amount of neighbours results in a noisy simulation (table 2, SIM1). The contrary leads to a downsampling of the generated segments that become longer than the interpreted fractures in AP3 (table 2, SIM7). Decreasing the acceptance threshold leads to an increase of the simulation time (table 2 SIM8-15). Increasing the scanned fraction of the TI is the most time consuming operation (table 2 SIM17-27).

Increasing the number of neighbours only is generally not sufficient to accurately generate a satisfactory or acceptable total amount of fractures (table 3). Increasing the scanned fraction of the TI produces in all cases the closest total number of fractures compared to the reference outcrop (table 3).

The counting of fractures in simulation zones revealed that set 2 and set 3 in zone 1, set 3 in zone 4 and set 1 in zone 5 are generally underestimated during the simulation process. In contrast, fracture set 1 in zone 2 is generally overestimated. The consistency of the error over almost the entire set of simulations indicates an issue on the training image representation (table 4-6). Increasing the scanned fraction of the TI generally allows to better represent a low proportion of fracture facies within a TI (Zone TI5, set 2, table 6).

An acceptance threshold below 5% leads to an overestimation of the number of small fractures (between 0-10 m), fig 8. In this case, amount of segments between 0-20 m is generally close to the reality. Increasing the scanned fraction of the TI produces the highest quantity of fractures ranging from 0-10 m (fig. 8). Increasing the number of neighbours and the percentage of the scanned TI will result in an increase of the length of the fractures used as hard conditioning data. However, the fracture elongation does not affect all of the hard conditioned fractures and represents a very small percentage of the whole modelled fracture network.

III.4.3 Attempt at an optimisation: OPT1

OPT1 was parameterised in regard of the previous observations in order to generate a simulation that is the closest-to-reality possible. For this purpose, the amount of fractures from set 2 and set 3 drawn in TI1 and set 3 drawn in TI4 was increased. In contrast, the amount of fractures from set 1 drawn in TI2 was decreased significantly (fig. 9). We choose to setup the number of neighbours at 50 and the acceptance threshold at 2%. TI1 and TI4 will be scanned at 75% and the rest of the TIs will be scanned at 50% (table 2).

The simulation time for the proposed simulation is 2 min 31s (table 2). The total amount of generated fractures is satisfactory compared to the amount of fractures interpreted in the original outcrop.

To evaluate the robustness of the optimised simulation, 6 realisations using the same parametrisation were generated for OPT1. The total amount of fractures generated for these simulations always fall below the 10% deviation compared to the reference outcrop.

The number of segments comprised between 0-20 m in OPT1 is slightly above the satisfactory deviation limit. As per all the generated simulations, the number of fractures between 2.21 m and 10 m is largely overestimated.

OPT1 contains a more satisfactory and acceptable fracture count than any other simulation generated before (table 6). The amount of segments generated in zone 1 and 2 for set 1 is slightly overestimated. In zone 3, OPT1 fails to represent the amount of fractures for set 1 (25% deviation) and for set 3. Fracture set 1 in zone 4 is largely overestimated.

III.4.4 Evaluation of the AP3 and OPT1 simulations: P_{2l} calculations

Uncertainty analysis is required when performing simulations of geological parameters, especially far from data. The sensitivity analysis presented in this paper is a way to compare the MPS simulations with the reference outcrop.

To reinforce the evaluation of the proposed method, we quantified the values of fracture intensity in the reference outcrop, in three selected AP3 MPS simulations and in the optimised simulation (OPT1) (fig. 10). The fracture intensity was classified by (Dershowitz and Herda, 1992) in regard of i) the size and dimension (1D, 2D, 3D) of a selected zone of interest and ii) the number, length, area or volume of fractures within this selected zone. In this paper, we chose to calculate the P_{2I} fracture intensity, which corresponds to the sum of all fracture lengths within a regularly discretized space, with constant area boxes (10×10 m) covering the entire AP3 area of interest.

Visually, the results show an apparent higher P_{2I} intensity in the reference outcrop than in the simulations. However, zones of high intensity in the reference outcrop are generally well represented in SIM26 and in OPT1. This is in agreement with the results of the sensitivity analysis showing that SIM26 and OPT1 best represent the number of fractures present in the reference outcrop.

The average fracture intensity in each simulation has also been computed and confirms the observations conducted during the sensitivity analysis. SIM1 and SIM7 present the lowest average fracture intensity (0.095 m^{-1} and 0.079 m^{-1} respectively) and SIM26 and OPT1 present the highest fracture intensity (0.11 m^{-1} and 0.099 m^{-1} respectively). The average fracture intensity in the reference outcrop is higher than in any other simulations (0.126 m^{-1}). However, this value remains close to the ones obtained in SIM26 and OPT1.

The fact that the fractures have been simplified as straight lines in the simulations combined to a relatively small area of calculation (10×10 m) could be one element of explanation of the observed fracture intensity variation between the reference outcrop and SIM26 and OPT1. This analysis strengthens the results obtained during the sensitivity analysis and demonstrates the capacity of the MPS method to represent with a high fidelity the geometry of a fracture network.

552

553

III.4.5 Using the sensitivity analysis results to model AP4

554

555

556

557

558

559

560

561

562

563

564

565

566

567

568

569

570

571

572

573

574

575

576

As per AP3, AP4 present an intrinsic variability of the fracture network geometry. This outcrop was divided in 3 elementary zones (fig. 11A-B). According to AP4 partitioning, a probability map with sharp boundaries (fig. 11B) was created. For AP4, the configuration of the outcrop led to mask the area where no interpretation data were performed. In these particular zones a “no data value” was attributed and these masked areas were excluded during the modelling process. In AP4 three training images were created (fig. 11C). As per AP3, the size of the AP4 simulation grid was doubled compared to its original dimension (available in fig.11). In AP4, fractures longer than 40 meters were also considered as hard conditioning data. Here, less than 1.5% of the fractures are longer than 40m (fig. 11D). In AP4, long fractures were found in the 3 sets and mainly in the south-eastern part of the outcrop (fig. 11D, elementary zone 6). 11 N180 fractures (0.5% of the whole), 13 N150 fractures (0.6% of the whole) and 9 N090 fractures (0.4% of the whole) were digitized and integrated as conditioning data into the simulation.

Based on the results of the sensitivity analysis of AP3 we generated one simulation for the AP4 outcrop (fig. 12). The modelling parameters for SIM AP4-1 were selected as following: the number of neighbours was set up at 50 and the acceptance threshold at 2%. The 3 training images used in the simulation are presented in figure 12 and are considered as representative of the fracture arrangement in each region of the simulation. The scanning percentage of TI6 and TI7 was set up at 50%. The scanning percentage of TI8 was set up at 100%. With this configuration, the simulation lasts slightly more than 5 minutes. The fact of intensely scanning TI8 is probably responsible of this duration. The analysis was conducted on the total amount of segments generated and of segments per set of fractures. In AP4 the total number of segments is 1810. The simulation realises 1682 segments in total, which constitutes a

satisfactory result. The original AP4 presents 252 segments striking N150, 856 segments striking N180 and 702 segments striking N090. The results of simulation AP4-1 are always satisfactory or acceptable with 206 segments striking N150, 834 segments striking N180 and 642 segments striking N090. A detailed analysis was not conducted here because AP4 contains a lot of small fracture intersections (especially in the TI8 zone) and this makes the segment extraction a complex process. However, these results are promising for the future.

IV] Smooth transitions between elementary zones: towards reservoir scale models to manage uncertainties

The strength of the method proposed here relies on the use of a probability maps and on the opportunity to consider multiple training images in a single realisation to generate non-stationary models of fracture network geometries. In the case of AP3 and AP4, the probability maps are essentially constrained by the variation of geometry of the fracture networks observed on the geological interpretation made on the drone imagery. Consequently, the defined areas are pragmatically bounded and the nature of the limit between one zone and another is a sharp boundary.

AP3 and AP4 outcrops are separated by about 2.5 km and very little is known about the fracture network geometry between these two locations. Assuming that there is no major structural deformation (fold or faults) that may cause a change in fracture geometry at the close vicinity of the outcrop “reality”, the zones initially defined on the AP3 and AP4 outcrop can be extended to the limits of the reservoir-scale model boundaries (fig. 13). In this particular case, filling the gap between the two outcrops appears to define how the transition between one side of the simulation grid and the other should be determined.

Fractures are localised objects that do not need to be necessarily continuous from one simulation zone to another. The constant higher proportion of the non-fractured matrix facies

versus localised and thin fracture elements ensures the coherency and relative compatibility from one simulation region to another. The idea of the simulation grid region partitioning was re-evaluated and an alternative method, was proposed here. Contrarily to the definition of sharp boundaries in the probability maps used for AP3 and AP4, a probability map with smooth transitions is defined as follows. An ensemble of elementary zones covering a part of the simulation grid is defined. Each TI corresponds to one elementary zone, which is simulated using exclusively that TI. The probabilities in these zones are then set to one for a specific TI and to zero for the other TIs. The remaining part of the simulation grid is divided in transition zones, for which one has to define which TIs may be involved. In a transition zone, the probabilities of the involved TIs are set proportional to the inverse distance to the corresponding elementary zones. This process creates smooth transitions in low constrained area decreasing the influence of one TI towards another (from one elementary zone to another).

No faults or folds can be initially identified between AP3 and AP4 to condition the drawing of the probability map. In this case, a rectangular compartment representing a gradual probability transition to use the training image associated to one outcrop or to the other filled the blank space between the two outcrops. For instance, fig 13E shows in the Transition_Zone_1 a decreasing probability to use TI1 from left to right (i.e. zone 1 to zone 6) and conversely to use TI6 from right to left.

Recently, investigations conducted on the Rio Grande do Norte geological map (Angelim et al., 2006), demonstrated the presence of a fault crossing the simulation grid near the AP3 zone. This structure may explain the variability of fracture geometry from AP3 (EW stylolites and strong presence of conjugated NS/NW-SE system) to AP4 (EW stylolites associated to NS fracture system, the NW-SE conjugated system is here subordinate). Further geological investigations need to be conducted in this particular place to proof the influence of this fault

on the network geometry. However, fig 13F shows an alternative probability map taking into account this interpretation and present how flexible the probability map can be. The proposed method demonstrates its adaptability in various geological contexts.

V] A method to create a 3D DFN out of 2D MPS realisations

The MPS simulations presented in this paper are on the form of 2D pixelated maps. MATLAB codes were developed to extract starting and end point coordinates (georeferenced) of a series of aligned colored pixels that represent a fracture trace from these images. Transforming this output in geologically realistic 3D surfaces is not easy. Karimpouli et al., (2017) studied samples coming from coalbed methane reservoirs in the fractured Late Permian Bowen Basin in Australia. They realised multiple 2D and pseudo 3D images (i.e. orthogonal 2D images) and used the cross-correlation based simulation (CCSIM) to represent the internal organisation of coal cleats and the heterogeneity of the coal matrix in 3D. Their approach greatly improved the understanding of the internal complexity of coal samples and gives better results than classical DFN's based on averaged distributions. However, their method requires an important initial amount of information (i.e. CT scans slices used as training images) that is generally not available at a larger scale. The use of MPS in 3D seems particularly not suited for fracture network representation because: i) they require to associate fractures from 2D map view and from 2D section view (3D or pseudo-3D), ii) it appears difficult to consider isolated fractures in this type of approach and iii) in the subsurface fracture height and/or fracture length are generally unknown.

To Tackle these problems we choose to use multiple 2D MPS-generated fracture networks. In the presented approach, the 3D is obtained by extruding 3D fracture planes in fracture units (fig. 14). In this approach we consider that fractures are entirely bound to the units, which can appear as a limitation if isolated fractures occurs inside a layer. However, we can consider

variable levels of fracture units. Figure 14 presents an hypothetical scenario where red fractures are confined to a large fracture unit (FU1) crosscutting smaller ones (FU4 containing also smaller red fractures). In such a representation, one 2D planar simulation is required at each top mechanical unit to generate a new set of fractures.

In real-world subsurface configurations, mechanical units can be extracted from well logs (resistivity, density, lithology; Laubach et al., 2009). The fracture height distribution, referred as fracture stratigraphy (Hooker et al., 2013) requires here a particular attention and is difficult to extract from borehole data. In outcrops, the use of vertical cliffs adjacent to 2D horizontal pavement should be a way to evaluate these heights and to constrain the 3D model. In outcrops, the resort to vertical cliffs adjacent to 2D horizontal pavements is required to define fracture height. This method is already implemented in gOcad-SKUA software as a macro that extrudes planes of a single fracture family (i.e. all the red fractures in AP3) vertically into a bounded volume (fig. 14). More developments are in process to generate oblique planes and to be able to extrude planes in portions of the fracture sets.

V] Conclusions

In this paper a new method to predict the geometry of a natural fracture network using the multiple-point statistic algorithm is presented. The method provides stochastic realisation depicting a realistic non-stationary fracture network arrangement in 2D based on the use of multiple, simplified, small training images capturing the natural fracture attributes in specific zones defined by a probability map. Probability maps are adaptable and follow geological rules of fracture type and arrangement distribution specific to various tectonic contexts (i.e. faulting, folding and poor deformation context/no fault, no folds). We developed methods to be able to consider transition zones into the probability maps (e.g. zones far from hard data) that allow simulating fracture network geometry at a larger scale (i.e. reservoir scale).

The realisations obtained from 2D MPS constitute a statistical laboratory close enough to the reality to be tested in terms of fracture mechanical parameters and response to flow. Comparison between mechanical aperture calculation, fluid flow simulations conducted on both “reality” fracture network interpretations performed on drone imagery and series of MPS realisations gives similar results.

The method proposed here is applicable to all rock types and to a wide range of tectonic contexts. Initially calibrated using outcrop data, the method is fully adaptable to the subsurface in order to better characterise fractures in water, heat or hydrocarbon reservoirs. The challenge there, remains on the definition of the different training images on which the simulation is based. Very few data are generally available in the subsurface and geological rules need to be found to define the geological characteristics of the fracture network (orthogonal or conjugate network) and the associated fracture attributes (length, height, spacing, density, topology).

Acknowledgments

The authors want to thank ENI S.P.A. for the financial support of this research. Silvia Mittempergher from the University of Milano Bicocca is acknowledged for providing the code extracting segments from pixelated images. We would like also to thank the entire SEFRAC group for their interest in developing this method and for their valuable geological advices. Acknowledgements are extended to Philippe Renard from the University of Neuchâtel, to Hadi Hajibeygi from TU Delft and to Wilfried Tsobleack from Paradigm Geo for the constructive discussions we had together. Prof. Hilario Bezerra from the Universidade Federal do Rio Grande do Norte is acknowledged for providing datasets concerning Apodi area and for his advises on the local geology. We would like to thank Jan Kees Blom from the TU Delft for the improvement he provided to this manuscript. We thank the two anonymous

reviewers, Stephen Laubach, William Dershowitz and John Hooker for their very useful comments that greatly participated to improve this paper.

Appendix A

The DeeSse algorithm (Straubhaar et al., 2011) was used in this paper to reproduce existing fracture network interpreted from outcrop pavements. The following pseudocode developed by Oriani et al., (2017) have been modified to explain how the algorithm is processing the simulation of fracture. Specific terms can be found in section II.1 of the present paper. In our study the simulation follows a random path into the simulation grid. This grid is step by step populated by values (fracture facies in our case) sampled in the training image. The algorithm proceeds according to the following sequence :

1. Selection of a random location \mathbf{x} in the simulation grid that has not yet been simulated (and not corresponding to conditioning data points, already inserted in the grid).
2. To simulate $\mathbf{V}(\mathbf{x}) \rightarrow$ the fracture facies into the simulation grid: The pattern $\mathbf{d}_n(\mathbf{x}) = (\mathbf{x}_1, \mathbf{V}(\mathbf{x}_1)), \dots, (\mathbf{x}_n, \mathbf{V}(\mathbf{x}_n))$ formed by at most \mathbf{n} informed nodes the closest to \mathbf{x} is retrieved. If no neighbours is assigned (at the beginning of the simulation), $\mathbf{d}_n(\mathbf{x})$ will then be empty: in this case, assign the value $\mathbf{V}(\mathbf{y})$ of a random location \mathbf{y} in the TI to $\mathbf{V}(\mathbf{x})$, and repeat the procedure from the beginning.
3. Visit a random location \mathbf{y} in the TI and retrieve the corresponding data event $\mathbf{d}_n(\mathbf{y})$.
4. Compare $\mathbf{d}_n(\mathbf{x})$ to $\mathbf{d}_n(\mathbf{y})$ using a distance $\mathbf{D}(\mathbf{d}_n(\mathbf{x}), \mathbf{d}_n(\mathbf{y}))$ corresponding to a measure of dissimilarity between the two data events.
5. If $\mathbf{D}(\mathbf{d}_n(\mathbf{x}), \mathbf{d}_n(\mathbf{y}))$ is smaller than a user-defined acceptance threshold \mathbf{T} , the value of $\mathbf{V}(\mathbf{y})$ is assigned to $\mathbf{V}(\mathbf{x})$. Otherwise step 3 to step 5 are repeated until the value is assigned or an given fraction \mathbf{F} of the TI, is scanned.

6. if F is scanned, $V(\mathbf{x})$ is defined as $V(\mathbf{y})$, with \mathbf{y} the scanned location minimising the distance $D(dn(\mathbf{x}), dn(\mathbf{y}))$.
7. Repeat the whole procedure until all the simulation grid is informed.

Figure captions

Figure 1: Direct Sampling method workflow applied to fracture network modelling (modified from Meerschman et al., 2013).

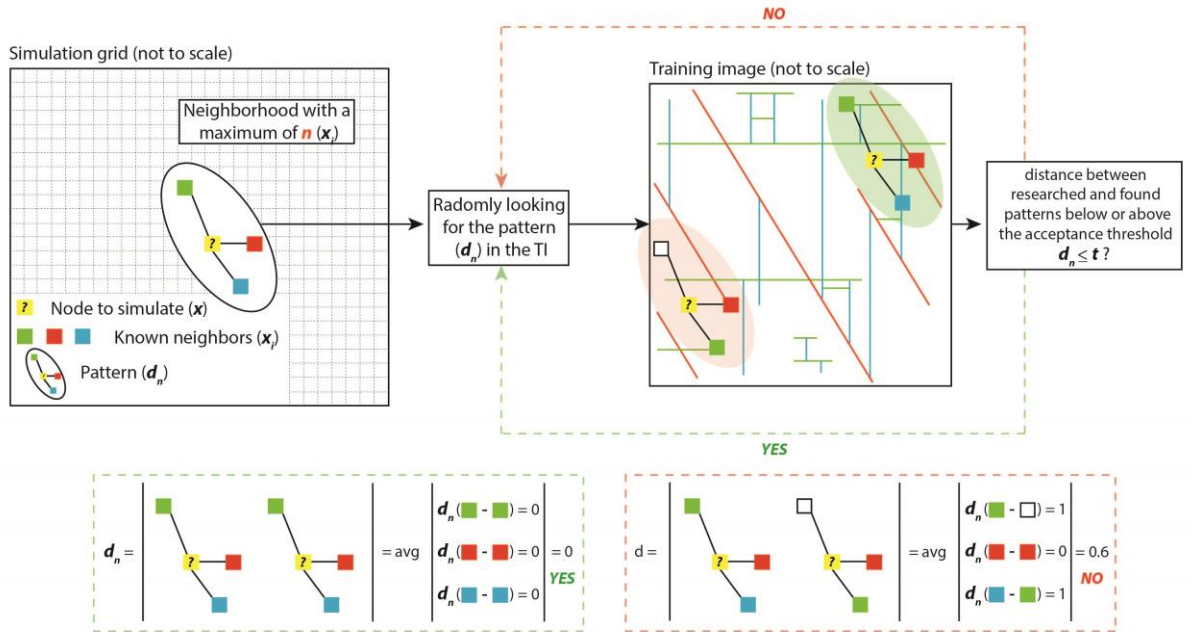
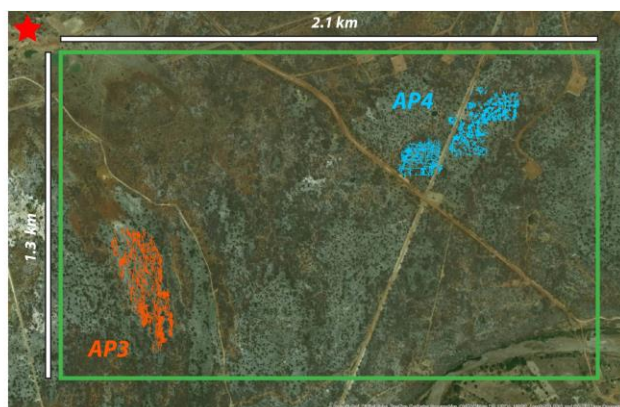
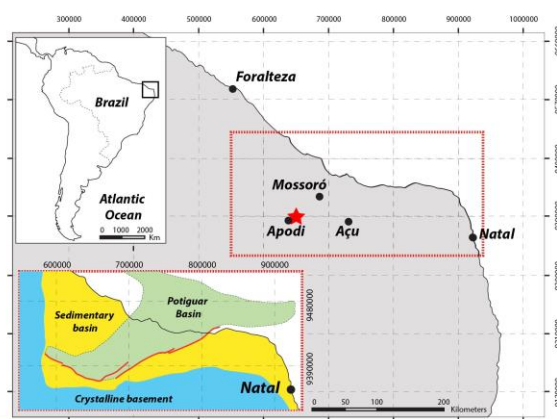


Figure 2: Location of the area of interest and of the studied pavements near Apodi area (red star).



738

739

740

741

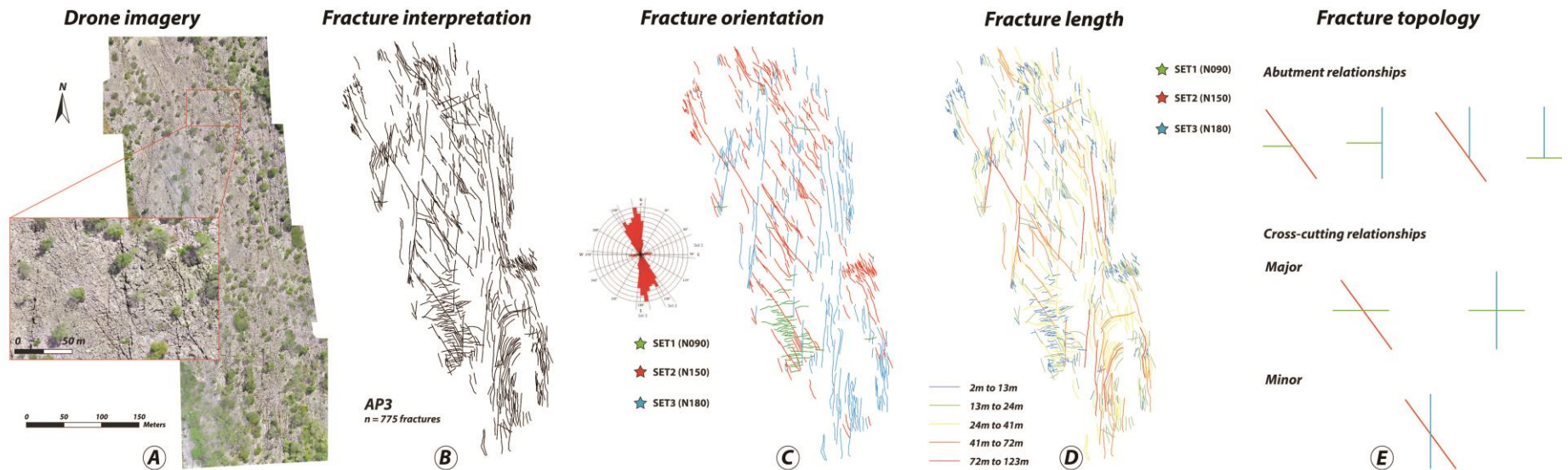
742

743 **Table 1:** Outcrop characteristics and fracture parameters collected in AP3 and AP4

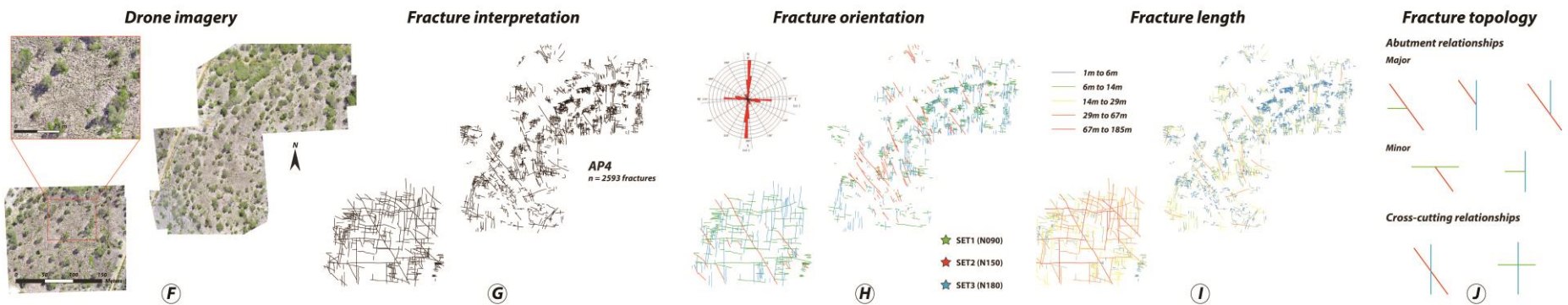
| AP3 outcrop | | | | | | | | | | | | | | | | | | | | | |
|-------------------------------|---------|-------------|-----------|--------|---|--------------------------|--------------------------|--------------------------|--------------------------|----------------------------|--------------------------|--------------------------|--------------------------|--------------------------|-------------------------|--------------------------|-------------------------|-------------------------|-------------------------|-----------------|---------|
| Localisation (WGS84 UTM Z24S) | | Orientation | Dimension | | Fractures proportion (of the whole fracture population) | | | | | | | | | | | | | | | Fracture length | |
| X | Y | | NS (m) | EW (m) | Set 1 (N135-N165) | | | | | Set 2 (N000-N010/N170-180) | | | | | Set3 (N075-N105) | | | | | Min (m) | Max (m) |
| 650601 | 9387908 | NNW-SSE | 600 | 300 | 30% | | | | | 52% | | | | | 18% | | | | | 2,21 | 123 |
| | | | | | Elementary zone 1 60% | Elementary zone 2 26% | Elementary zone 3 18% | Elementary zone 4 70% | Elementary zone 5 87% | Elementary zone 1 37% | Elementary zone 2 14% | Elementary zone 3 80% | Elementary zone 4 23% | Elementary zone 5 13% | Elementary zone 1 3% | Elementary zone 2 60% | Elementary zone 3 2% | Elementary zone 4 7% | Elementary zone 5 0% | | |

| AP4 outcrop | | | | | | | | | | | | | | | | | | | | | |
|-------------------------------|---------|-------------|-----------|--------|---|--------------------------|--------------------------|--------------------------|--------------------------|----------------------------|--------------------------|--------------------------|--------------------------|--|------------------|--|--|--|--|-----------------|---------|
| Localisation (WGS84 UTM Z24S) | | Orientation | Dimension | | Fractures proportion (of the whole fracture population) | | | | | | | | | | | | | | | Fracture length | |
| X | Y | | NS (m) | EW (m) | Set 1 (N135-N165) | | | | | Set 2 (N000-N010/N170-180) | | | | | Set3 (N075-N105) | | | | | Min (m) | Max (m) |
| 652032 | 9388508 | NE-Sw | 400 | 500 | 20% | | | | | 40% | | | | | 40% | | | | | 1 | 186 |
| | | | | | Elementary zone 6 8% | Elementary zone 7 20% | Elementary zone 8 10% | Elementary zone 6 43% | Elementary zone 7 45% | Elementary zone 8 53% | Elementary zone 6 49% | Elementary zone 7 35% | Elementary zone 8 37% | | | | | | | | |

756 **Figure 3:** Data acquired in the area of interest in pavements AP3. A) ortho-rectified high-resolution pavement aerial images acquired with a
757 drone, B) fracture interpretation on ortho-rectified images, C) fracture orientation calculated from the north in GIS-based environment.
758 Corresponding rose diagram for both outcrops, D) length of each fracture trace and E) fracture topology relationship for each pavement observed
759 on fracture network interpretation.



764 **Figure 4:** Data acquired in the area of interest in pavements AP4. F) ortho-rectified high-resolution pavement aerial images acquired with a
 765 drone, G) fracture interpretation on ortho-rectified images, H) fracture orientation calculated from the north in GIS-based environment.
 766 Corresponding rose diagram for both outcrops, I) length of each fracture trace and J) fracture topology relationship for each pavement observed
 767 on fracture network interpretation



774 **Figure 5:** A) Partitioning of AP3 in 5 elementary zones (EZ). This partition is defined (with
 775 respect to fracture orientation (fracture facies), fracture density and geometry variability over
 776 the entire simulation domain. B) probability map and associated statistics for each EZ. C)
 777 training images associated with the partition of AP3. In each EZ, the corresponding training
 778 image has a probability (pTI) of 1 to be used. In this zone the other training images are not
 779 used (pTI = 0). D) hard conditioning data for AP3. All the fractures longer than 40 m are
 780 considered deterministically in the simulation process

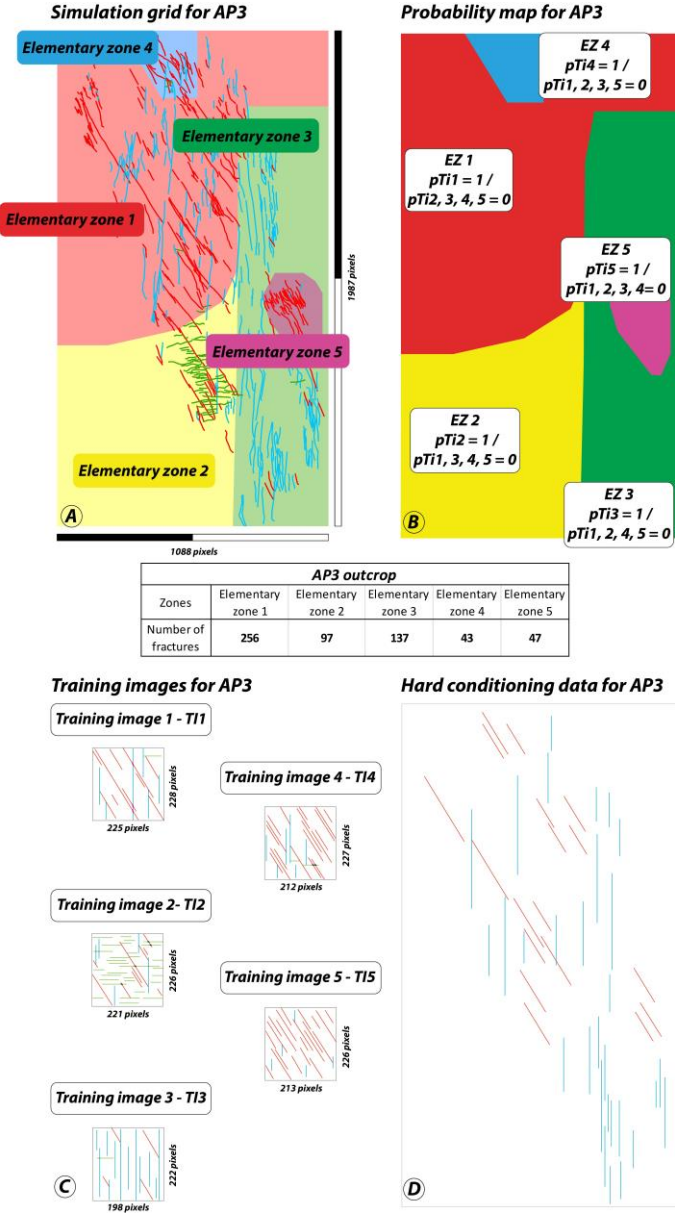


Figure 6: Comparison between results obtained without constraining the topology and with topological facies constraints.

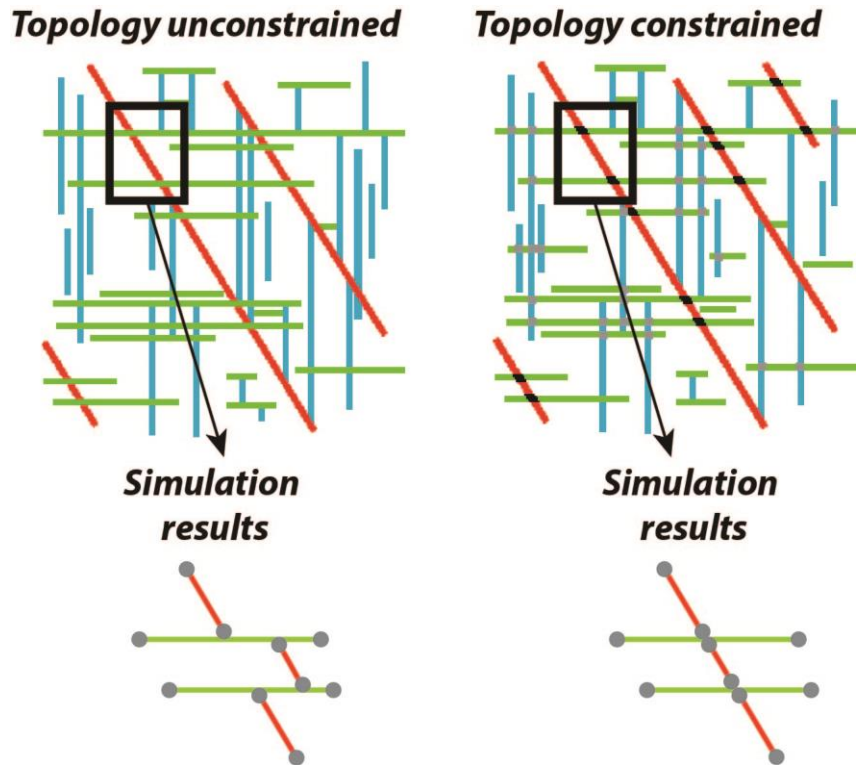


Figure 7: Visual comparison between: A) the reference fracture network interpretation (AP3), B) the extraction of the longer segments (50 fracture longer than 40m), C) a simulation conditioned by the long segments, D) a simulation not conditioned by the long segments

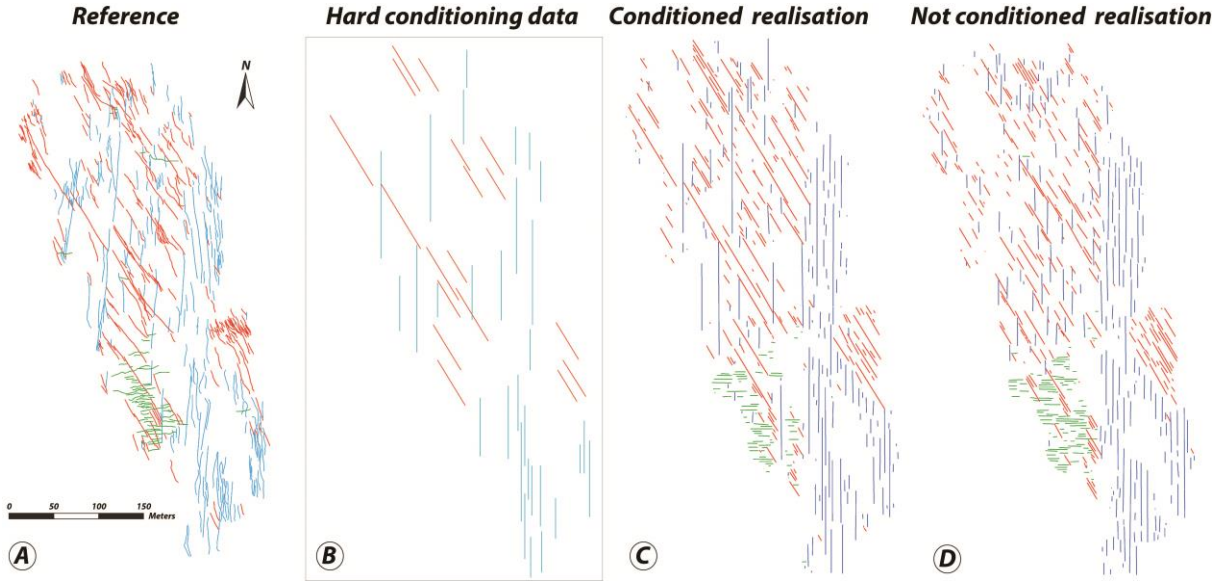


Table 2: Simulation parametrisation, models set-ups and duration (in seconds) of each run.

| Tested parametrisation | Number of neighbours influence | | | | | | | Number of neighbours + Acceptance threshold | | | | | | | |
|------------------------|--------------------------------|----------|----------|----------|----------|----------|-----------|---|----------|----------|----------|----------|----------|----------|----------|
| Realisation name | SIM1 | SIM2 | SIM3 | SIM4 | SIM5 | SIM6 | SIM7 | SIM8 | SIM9 | SIM10 | SIM11 | SIM12 | SIM13 | SIM14 | SIM15 |
| Simulation parameters | A. th. = | A. th. = | A. th. = | A. th. = | A. th. = | A. th. = | A. th. = | A. th. = | A. th. = | A. th. = | A. th. = | A. th. = | A. th. = | A. th. = | A. th. = |
| | 5% N. = | 5% N. = | 5% N. = | 5% N. = | 5% N. = | 5% N. = | 5% N. = | 4% N. = | 3% N. = | 2% N. = | 1% N. = | 4% N. = | 3% N. = | 2% N. = | 1% N. = |
| | 10 Scan= | 20 Scan= | 30 Scan= | 40 Scan= | 50 Scan= | 75 Scan= | 100 Scan= | 40 Scan= | 40 Scan= | 40 Scan= | 40 Scan= | 50 Scan= | 50 Scan= | 50 Scan= | 50 Scan= |
| | 25% | 25% | 25% | 25% | 25% | 25% | 25% | 25% | 25% | 25% | 25% | 25% | 25% | 25% | 25% |
| Simulation duration | 22" | 19" | 33" | 36" | 55" | 101" | 136" | 52" | 52" | 90" | 95" | 56" | 76" | 76" | 121" |

| Tested parametrisation | Number of neighbours + Acceptance threshold + % TI scan | | | | | | | | | | | | Optimisation |
|------------------------|---|----------|----------|----------|----------|----------|----------|----------|----------|----------|----------|----------|--------------|
| Group | Group 1 | | | | Group 2 | | | | Group3 | | | | |
| Realisation name | SIM16 | SIM17 | SIM18 | SIM19 | SIM20 | SIM21 | SIM22 | SIM23 | SIM24 | SIM25 | SIM26 | SIM27 | OPT1 |
| Simulation parameters | A. th. = | A. th. = | A. th. = | A. th. = | A. th. = | A. th. = | A. th. = | A. th. = | A. th. = | A. th. = | A. th. = | A. th. = | Custom |
| | 3% N. = | 2% N. = | 3% N. = | 2% N. = | 3% N. = | 2% N. = | 3% N. = | 2% N. = | 3% N. = | 2% N. = | 3% N. = | 2% N. = | |
| | 40 Scan= | 40 Scan= | 50 Scan= | 50 Scan= | 40 Scan= | 40 Scan= | 50 Scan= | 50 Scan= | 40 Scan= | 40 Scan= | 50 Scan= | 50 Scan= | |
| | 50% | 50% | 50% | 50% | 75% | 75% | 75% | 75% | 100% | 100% | 100% | 100% | |
| Simulation duration | 80" | 148" | 123" | 124" | 105" | 196" | 152" | 154" | 104" | 203" | 150" | 149" | 151" |

Table 3: Comparison between the total amount of segments interpreted in the reference outcrop and in the different sets of simulations (tested parametrisation). Evaluation of the results in terms of satisfactory (green symbol), acceptable (orange symbol) or non-satisfactory (red symbol)

| | | | | Results evaluation | | |
|----------------|-------------------|---|---------------------------------|--------------------|---|---|
| | Reference outcrop | Tested Parametrisation | Number of tested configurations | ✓ | ≈ | ✗ |
| Total segments | 562 | Influence of the number of neighbours | n=7 | 1 | 1 | 5 |
| | | Number of neighbours + Acceptance threshold | n=8 | 3 | 2 | 3 |
| | | Number of neighbours + Acceptance threshold + % TI scan | n=12 | 5 | 6 | 1 |

Table 4: Results of the sensitivity analysis on the influence of the number of neighbours. The table presents the number of segments per simulation zone for AP3 (used as reference). Red symbols show a total amount of segments of the considered set in the considered zone deviating to more than 20% from the reference case. Yellow symbols show a deviation of more than 10% from the reference case. Green symbols do not deviate significantly from the reference outcrop interpretation.

| | | | <i>Number of neighbours</i> | | | | | | |
|---------------------------|-------------|---------------------------|-----------------------------|-------------|-------------|-------------|-------------|-------------|-------------|
| | | <i>Reference</i> | <i>SIM1</i> | <i>SIM2</i> | <i>SIM3</i> | <i>SIM4</i> | <i>SIM5</i> | <i>SIM6</i> | <i>SIM7</i> |
| <i>Segments per parts</i> | | | | | | | | | |
| Zone T11 | Set1 | 156 | ✗ | ≈ | ≈ | ✗ | ✗ | ✗ | ✗ |
| | Set2 | 95 | ✗ | ✗ | ≈ | ✗ | ✗ | ✗ | ✗ |
| | Set3 | 6 | ✗ | ✗ | ✗ | ✗ | ✗ | ✗ | ✗ |
| Zone T12 | Set1 | 22 | ✗ | ✗ | ✗ | ✗ | ✗ | ✗ | ≈ |
| | Set2 | 12 | ✗ | ✗ | ✓ | ✗ | ✗ | ✗ | ✗ |
| | Set3 | 57 | ✗ | ≈ | ✓ | ✓ | ✓ | ≈ | ✓ |
| Zone T13 | Set1 | 20 | ✗ | ✓ | ✗ | ✗ | ✗ | ✗ | ✗ |
| | Set2 | 113 | ✗ | ≈ | ✓ | ≈ | ≈ | ✗ | ✗ |
| | Set3 | 2 | ✗ | ✗ | ✗ | ≈ | ≈ | ✗ | ✗ |
| Zone T14 | Set1 | 25 | ✗ | ✗ | ✗ | ✓ | ✓ | ≈ | ✗ |
| | Set2 | 10 | ✓ | ✓ | ✓ | ✓ | ≈ | ≈ | ≈ |
| | Set3 | 3 | ✗ | ✗ | ✗ | ✗ | ✗ | ✗ | ≈ |
| Zone T15 | Set1 | 39 | ✓ | ≈ | ✗ | ✗ | ✗ | ✗ | ✗ |
| | Set2 | 2 | ✗ | ✗ | ✗ | ✗ | ✓ | ✓ | ≈ |
| | Set3 | 0 | ✓ | ✓ | ✓ | ✓ | ✓ | ✓ | ✓ |
| | | Satisfactory total | No | Yes | Yes | No | No | No | No |
| | | # satisfactory | 3 | 3 | 5 | 4 | 4 | 2 | 4 |
| | | # acceptable | 0 | 4 | 2 | 2 | 3 | 3 | 2 |
| | | # not acceptable | 12 | 8 | 8 | 9 | 8 | 10 | 9 |

Table 5: Results of the sensitivity analysis on the influence of the number of neighbours and of the variation of the acceptance threshold. The colour code is the same as the one used in table 4.

| | | | Number of neighbours + Acceptance threshold | | | | | | | |
|--------------------|------|-----|---|------|-------|-------|-------|-------|-------|-------|
| Reference | | | SIM8 | SIM9 | SIM10 | SIM11 | SIM12 | SIM13 | SIM14 | SIM15 |
| Segments per parts | | | | | | | | | | |
| Zone TI1 | Set1 | 156 | ✓ | ✓ | ≈ | ≈ | ✗ | ✓ | ✓ | ✓ |
| | Set2 | 95 | ✗ | ✗ | ✗ | ✗ | ✗ | ✗ | ✗ | ✗ |
| | Set3 | 6 | ✗ | ✗ | ✗ | ✗ | ✗ | ✗ | ✗ | ✗ |
| Zone TI2 | Set1 | 22 | ✗ | ✗ | ✗ | ✗ | ✗ | ✗ | ✗ | ✗ |
| | Set2 | 12 | ≈ | ≈ | ✓ | ✓ | ✗ | ✗ | ✗ | ✗ |
| | Set3 | 57 | ✓ | ✓ | ✗ | ✗ | ✓ | ✓ | ✓ | ≈ |
| Zone TI3 | Set1 | 20 | ✗ | ✗ | ✓ | ✓ | ✗ | ✗ | ✗ | ✗ |
| | Set2 | 113 | ✓ | ✓ | ≈ | ≈ | ≈ | ✓ | ✓ | ≈ |
| | Set3 | 2 | ≈ | ≈ | ✓ | ✓ | ≈ | ✗ | ✗ | ✓ |
| Zone TI4 | Set1 | 25 | ✓ | ✓ | ✗ | ✗ | ✓ | ✓ | ✓ | ✓ |
| | Set2 | 10 | ✗ | ✗ | ≈ | ≈ | ≈ | ≈ | ≈ | ✓ |
| | Set3 | 3 | ✗ | ✗ | ✗ | ✗ | ✗ | ✗ | ✗ | ✗ |
| Zone TI5 | Set1 | 39 | ✗ | ✗ | ✗ | ✗ | ✗ | ✗ | ✗ | ✗ |
| | Set2 | 2 | ≈ | ≈ | ≈ | ≈ | ✓ | ≈ | ≈ | ≈ |
| | Set3 | 0 | ✓ | ✓ | ✓ | ✓ | ✓ | ✓ | ✓ | ✓ |
| Satisfactory total | | | Yes | Yes | Yes | Yes | No | No | No | Yes |
| # satisfactory | | | 5 | 5 | 4 | 4 | 4 | 5 | 5 | 5 |
| # acceptable | | | 3 | 3 | 4 | 4 | 6 | 2 | 2 | 3 |
| # not acceptable | | | 7 | 7 | 7 | 7 | 9 | 8 | 8 | 7 |

Table 6: Results of the sensitivity analysis on the influence of the number of neighbours, of the variation of the acceptance threshold and of the variation of the percentage of the scanned fraction of the training image. The colour code is the same as the one used in table

| | | | Number of neighbours + Acceptance threshold + % TI scan | | | | | | | | | | | | Optimisation |
|--------------------|-----------|--------------------|---|-------|-------|-------|---------|-------|-------|-------|--------|-------|-------|-------|--------------|
| | | | Group 1 | | | | Group 2 | | | | Group3 | | | | |
| | Reference | | SIM16 | SIM17 | SIM18 | SIM19 | SIM20 | SIM21 | SIM22 | SIM23 | SIM24 | SIM25 | SIM26 | SIM27 | OPT1 |
| Segments per parts | | | | | | | | | | | | | | | |
| Zone TI1 | Set1 | 156 | | ✓ | ✓ | ✓ | ✓ | ✗ | ✓ | ✓ | ✓ | ✗ | ✓ | ✓ | ✗ |
| | Set2 | 95 | | ✗ | ✗ | ✗ | ✗ | ≈ | ✗ | ✗ | ✗ | ≈ | ✗ | ✗ | ✓ |
| | Set3 | 6 | | ✗ | ✗ | ✗ | ✗ | ✗ | ✗ | ✗ | ✗ | ✗ | ✗ | ✗ | ✓ |
| Zone TI2 | Set1 | 22 | | ✗ | ✗ | ✗ | ✗ | ✗ | ✗ | ✗ | ✗ | ✗ | ✗ | ✗ | ✗ |
| | Set2 | 12 | | ✗ | ✗ | ✗ | ✗ | ✗ | ✗ | ✗ | ✓ | ✗ | ✓ | ✓ | ✓ |
| | Set3 | 57 | | ✓ | ✓ | ✓ | ✓ | ≈ | ✓ | ✓ | ✓ | ≈ | ✓ | ✓ | ≈ |
| Zone TI3 | Set1 | 20 | | ✗ | ✗ | ✗ | ✓ | ✗ | ✗ | ✗ | ≈ | ✗ | ✓ | ✓ | ✗ |
| | Set2 | 113 | | ✓ | ✓ | ✓ | ≈ | ✓ | ✓ | ✓ | ✓ | ✓ | ≈ | ≈ | ✓ |
| | Set3 | 2 | | ≈ | ≈ | ≈ | ✗ | ✓ | ✓ | ✓ | ≈ | ≈ | ✗ | ✗ | ✗ |
| Zone TI4 | Set1 | 25 | | ✗ | ✗ | ✗ | ≈ | ✗ | ✓ | ✓ | ✗ | ✗ | ≈ | ≈ | ✗ |
| | Set2 | 10 | | ✓ | ✓ | ✓ | ≈ | ✓ | ✓ | ✓ | ✗ | ≈ | ✓ | ✓ | ✓ |
| | Set3 | 3 | | ✗ | ✗ | ✗ | ✗ | ✗ | ✗ | ✗ | ✗ | ≈ | ✗ | ✗ | ✓ |
| Zone TI5 | Set1 | 39 | | ≈ | ≈ | ≈ | ✗ | ✗ | ✗ | ✗ | ✓ | ≈ | ✗ | ✗ | ≈ |
| | Set2 | 2 | | ≈ | ≈ | ≈ | ✗ | ✗ | ✓ | ✓ | ≈ | ≈ | ✓ | ✓ | ✓ |
| | Set3 | 0 | | ✓ | ✓ | ✓ | ✓ | ✓ | ✓ | ✓ | ✓ | ✓ | ✓ | ✓ | ✓ |
| | | Satisfactory total | | Yes | Yes | Yes | No | No | Yes | Yes | Yes | Yes | Yes | Yes | Yes |
| | | # satisfactory | | 5 | 5 | 5 | 4 | 4 | 8 | 8 | 6 | 2 | 7 | 7 | 8 |
| | | # acceptable | | 3 | 3 | 3 | 3 | 2 | 0 | 0 | 3 | 7 | 2 | 2 | 2 |
| | | # not acceptable | | 7 | 7 | 7 | 8 | 9 | 7 | 7 | 6 | 6 | 6 | 6 | 5 |

830 **Figure 8:** Fracture length distributions tested during the sensitivity analysis. A) fracture
 831 length distribution for SIM1 to SIM7, B) fracture length distribution for SIM10, SIM12,
 832 SIM13, SIM15 and C) fracture length distribution for SIM16, SIM17, SIM20, SIM21, SIM22,
 833 SIM24, SIM5, SIM26.

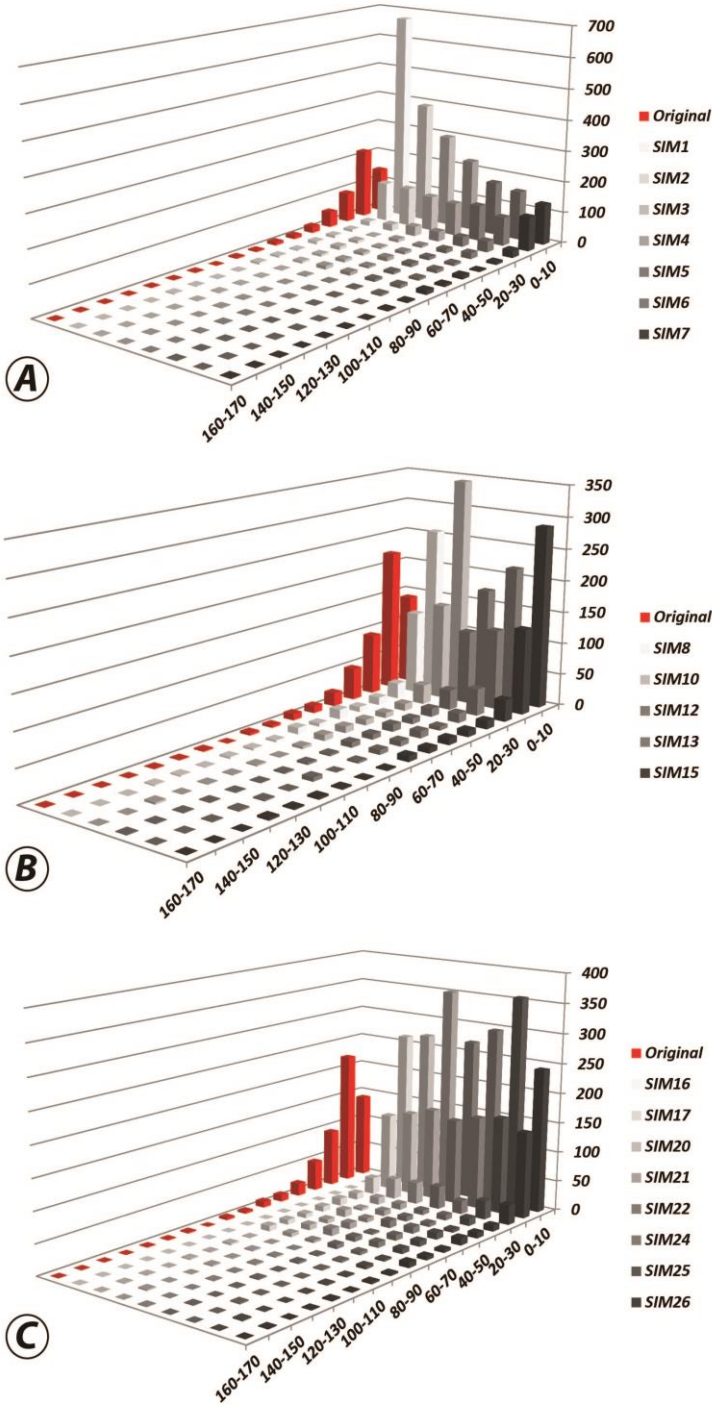


Figure 9: Comparison of the training images 1, 3 and 4 used during the sensitivity analysis (27 simulations) and their modification for SIM 3

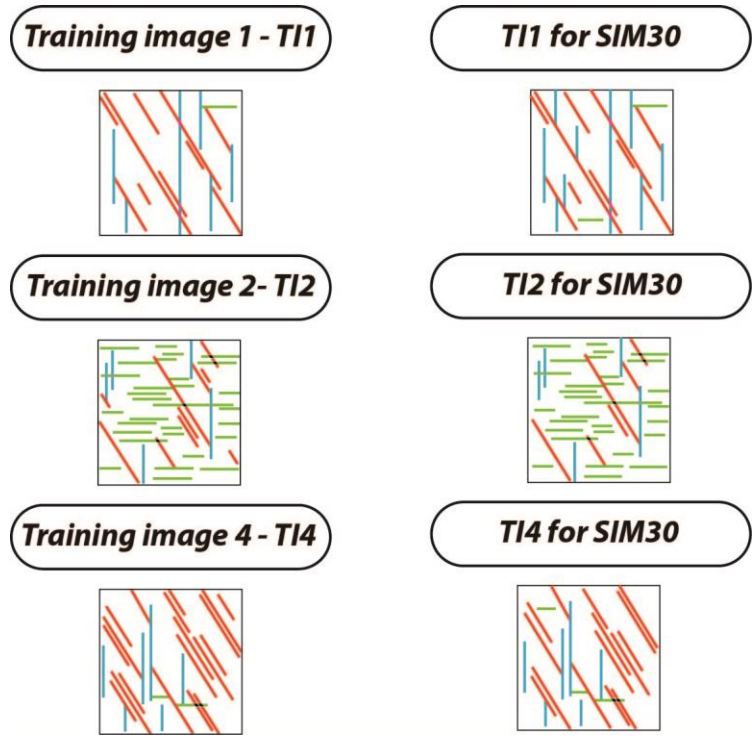


Figure 10: Comparison of the fracture intensity (P_{21}) calculated in the reference outcrop and in four select MPS simulations

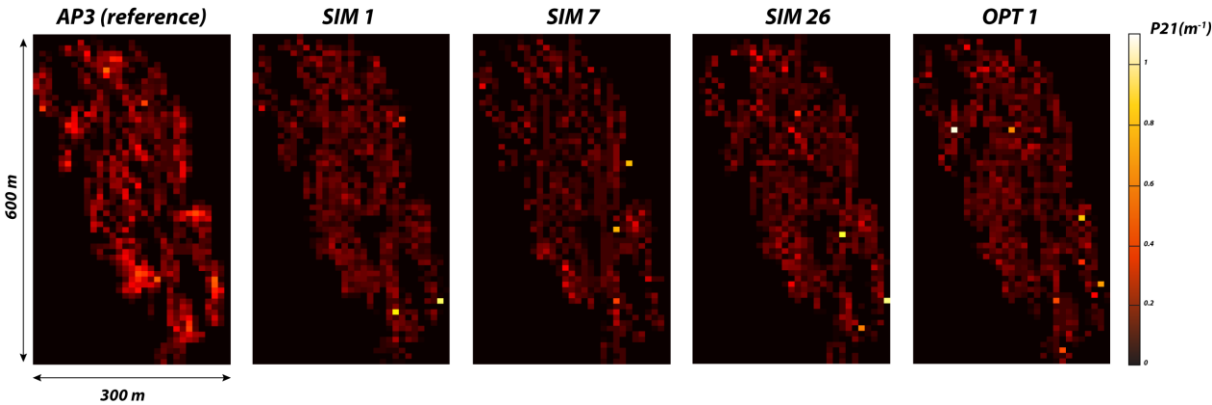


Figure 11: A) Partitioning of AP4 in 3 EZ. B) probability map and associated statistics for each EZ. C) training images associated with the partition of AP4. D) hard conditioning data for AP4

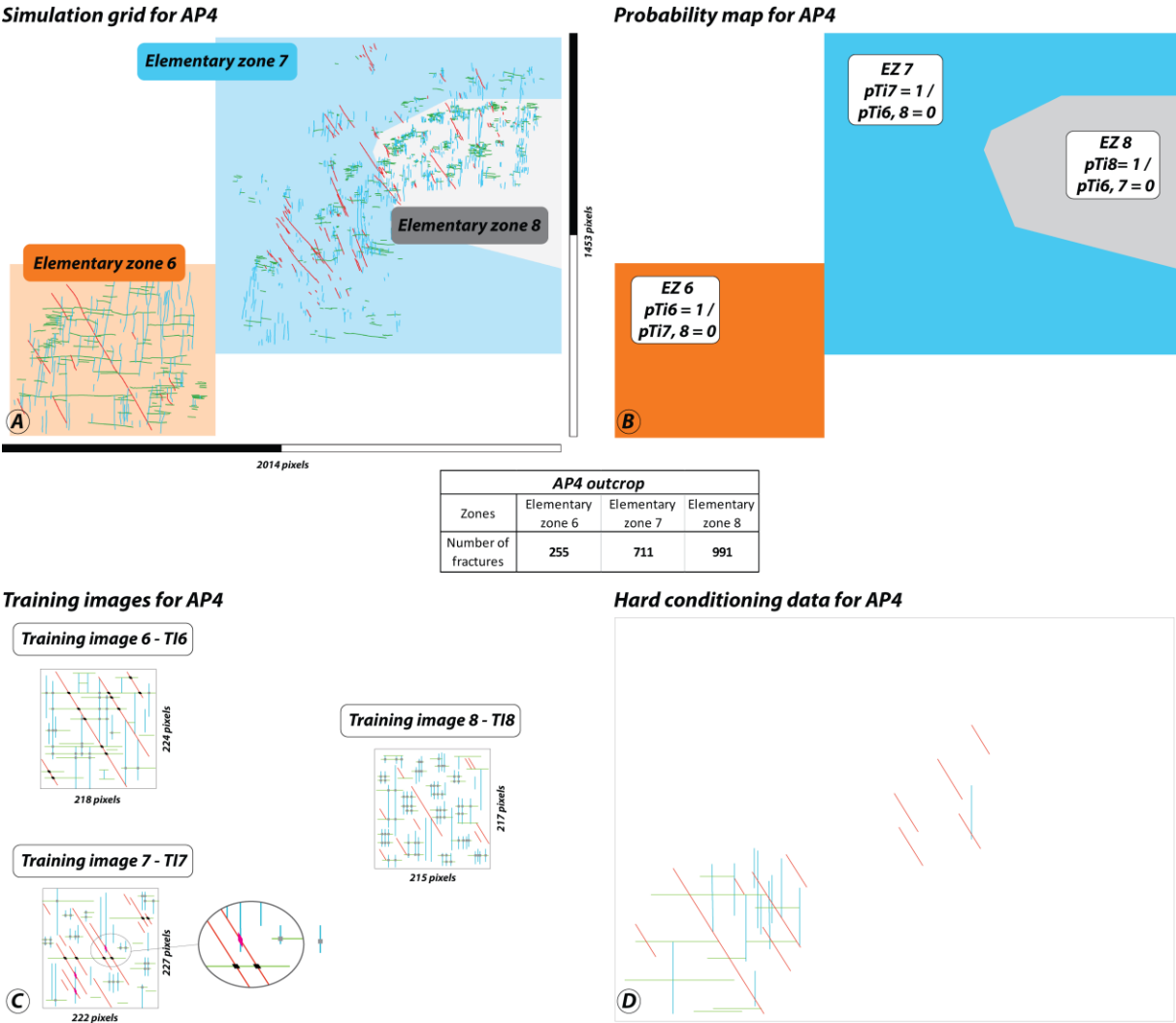


Figure 12: Comparison of the AP4 original outcrop with a MPS simulated version AP4-1

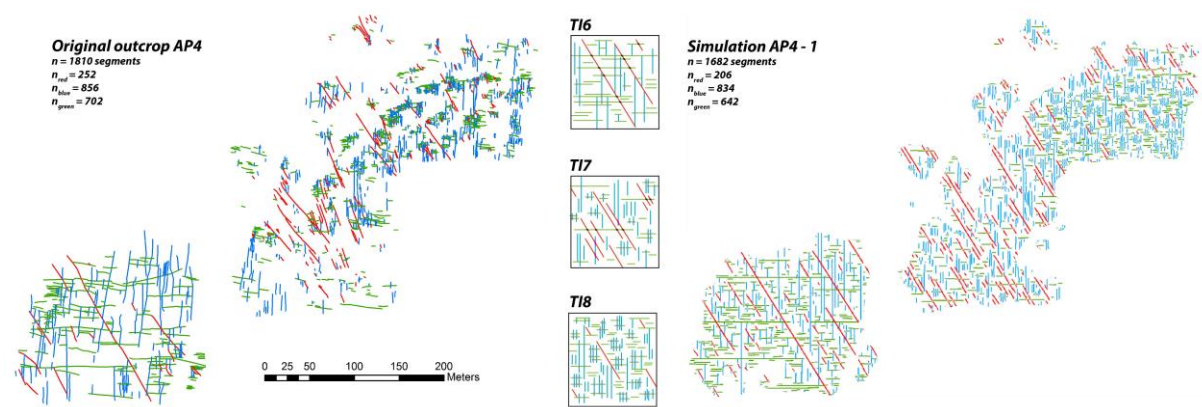


Figure 13: Smooth probability map at the reservoir scale (combination of AP3 and AP4). A) Relative position of AP3 and AP4 outcrops. B) Apodi fault added into the area of interest. Extension of the probability map regions in AP3 and AP4 without geological drivers C) and with the influence of the Apodi fault D). Probability maps with smooth transition zones without geological drivers E) and with the influence of the Apodi fault F).

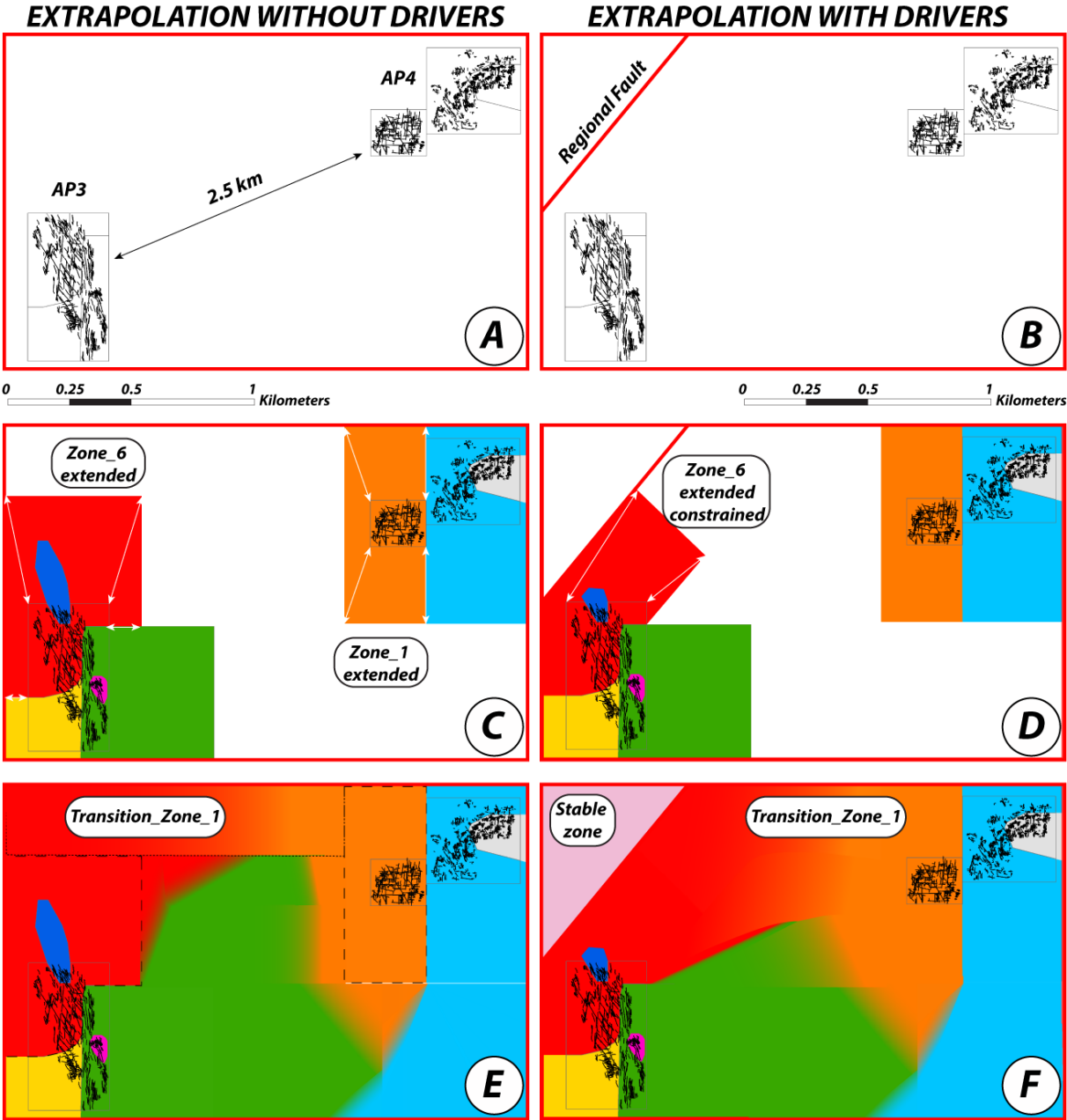
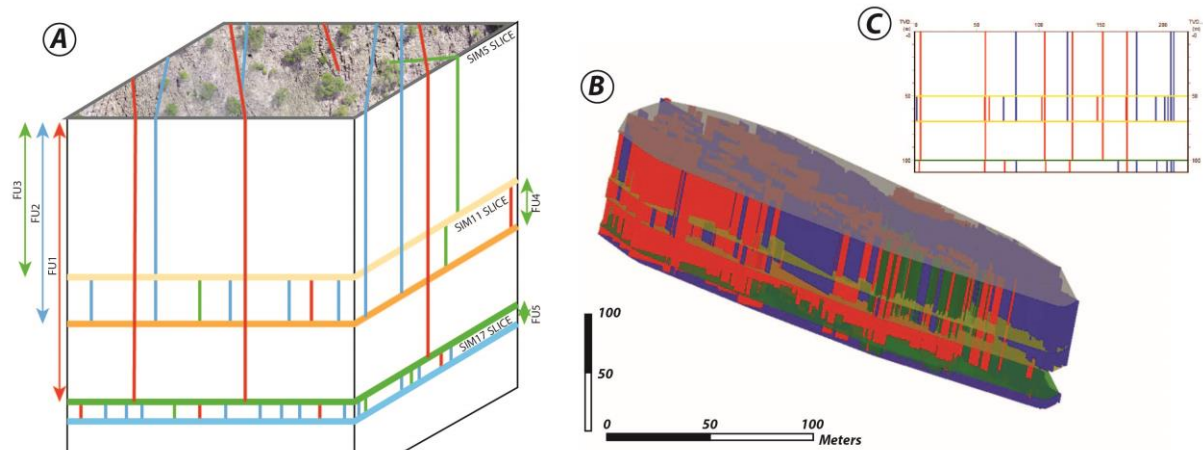


Figure 14: Fracture network extrusion in 3D. The method consists of identifying the different fracture units (FU) on which the fracture height is supposed to be constant (A). This method requires one simulation per top fracture unit (SIM SLICES). (B) is a 3D DFN based on the hypothetical case (A) and realised in gOcad software. (C) is a cross section realised in the centre of the 3D model in the E-W direction.



References

- Agar, S. M. and Geiger, S.: Fundamental controls on fluid flow in carbonates: current workflows to emerging technologies, Geological Society, London, Special Publications, 406, 60, 2015.
- Angelim, L. A. A., Medeiros, V. C., and Nesi, J. R.: Mapa geológico do Estado do Rio Grande do Norte, CPRM/FAPERN, Recife, Projeto Geologia e Recursos Minerais do Estado do Rio Grande do Norte, 2006.
- Bemis, S. P., Mickelthwaite, S., Turner, D., James, M. R., Akciz, S., Thiele, S. T., and Bangash, H. A.: Ground-based and UAV-Based photogrammetry: A multi-scale, high-resolution mapping tool for structural geology and paleoseismology, *Journal of Structural Geology*, 69, 163-178, 2014.
- Berkowitz, B.: Characterizing flow and transport in fractured geological media: A review, *Advances in Water Resources*, 25, 861-884, 2002.
- Bertotti, G., de Graaf, S., Bisdorn, K., Oskam, B., Vonhof, H. B., Bezerra, F. H. R., Reijmer, J. J. G., and Cazarin, C. L.: Fracturing and fluid-flow during post-rift subsidence in carbonates of the Jandaira Formation, Potiguar Basin, NE Brazil, *Basin Research*, 29, 18, 2017.
- Bisdorn, K.: Burial-related fracturing in sub-horizontal and folded reservoirs - Geometry, geomechanics and impact on permeability, Doctorate, Technische Universiteit Delft, 2016.
- Bisdorn, K., Gauthier, B. D. M., Bertotti, G., and Hardebol, N. J.: Calibrating discrete fracture-network models with a carbonate three-dimensional outcrop fracture network: Implications for naturally fractured reservoir modeling, *AAPG Bulletin*, 98, 1351-1376, 2014.
- Bisdorn, K., Nick, H. M., and Bertotti, G.: An integrated workflow for stress and flow modelling using outcrop-derived discrete fracture networks, *Computers & Geosciences*, 103, 21-35, 2017.
- Bruna, P.-O., Guglielmi, Y., Viseur, S., Lamarche, J., and Bildstein, O.: Coupling fracture facies with in-situ permeability measurements to generate stochastic simulations of tight carbonate aquifer properties: Example from the Lower Cretaceous aquifer, Northern Provence, SE France, *Journal of Hydrology*, 529, Part 3, 737-753, 2015.
- Bruna, P.-O., Hardebol, N., Bisdorn, K., Straubhaar, J., Mariethoz, G., and Bertotti, G.: 2D to 3D fracture network detection and forecasting in a carbonate reservoir analogue using Multiple Point Statistics (MPS). ExCEL London 2017.
- Bruna, P.-O., Prabhakaran, R., Bertotti, G., Mittempergher, S., Succo, A., Bistacchi, A., Storti, F., and Meda, M.: Multiscale 3D prediction of fracture network geometry and fluid flow efficiency in folded carbonate reservoir analogues; Case study of the Island of Pag (Croatia). Muscat, Oman, 5-7 February 2018 2018.
- Chopra, S. and Marfurt, K. J.: Volumetric curvature attributes for fault/fracture characterization, *First Break*, 25, 12, 2007.
- Chugunova, T., Corpel, V., and Gomez, J.-P.: Explicit fracture network modelling: from multiple point statistics to dynamic simulation, *Mathematical Geosciences*, 49, 13, 2017.
- Chugunova, T. L. and Hu, L. Y.: Multiple-Point Simulations Constrained by Continuous Auxiliary Data, *Mathematical Geosciences*, 40, 133-146, 2008.
- Claes, H., Degros, M., Soete, J., Claes, S., Kele, S., Mindszenty, A., Török, Á., El Desouky, H., Vanhaecke, F., and Swennen, R.: Geobody architecture, genesis and petrophysical characteristics of the Budakalász travertines, Buda Hills (Hungary), *Quaternary International*, 437, 107-128, 2017.
- Corradetti, A., Tavani, S., Parente, M., Iannace, A., Vinci, F., Pirmez, C., Torrieri, S., Giorgioni, M., Pignalosa, A., and Mazzoli, S.: Distribution and arrest of vertical through-going joints in a

979 seismic-scale carbonate platform exposure (Sorrento peninsula, Italy): insights from
 980 integrating field survey and digital outcrop model, *Journal of Structural Geology*, doi:
 981 <https://doi.org/10.1016/j.jsg.2017.09.009>, 2017a. 2017a.

982 Corradetti, A., Tavani, S., Russo, m., Arbues, P. C., and Granado, P.: Quantitative analysis of
 983 folds by means of orthorectified photogrammetric 3D models: A case study from Mt. Catria,
 984 Northern Apennines, Italy, *The photogrammetric record*, doi: 10.1111/phor.12212, 2017b.
 985 17, 2017b.

986 Costa de Melo, A. C., de Castro, D. L., Bezerra, F. H. R., and Bertotti, G.: Rift fault geometry
 987 and evolution in the Cretaceous Potiguar Basin (NE Brazil) based on fault growth models,
 988 *Journal of South American Earth Sciences*, 71, 96-107, 2016.

989 Council, N. R.: *Rock Fractures and Fluid Flow: Contemporary Understanding and*
 990 *Applications*, The National Academies Press, Washington, DC, 1996.

991 de Brito Neves, B. B., Fuck, R. A., Cordani, U. G., and Thomaz F°, A.: Influence of basement
 992 structures on the evolution of the major sedimentary basins of Brazil: A case of tectonic
 993 heritage, *Journal of Geodynamics*, 1, 495-510, 1984.

994 Dershowitz, W. S. and Herda, H.: *Interpretation of Fracture Spacing and Intensity*,
 995 Balkema 1992.

996 Deutsch, C. V. and Journel, A. G.: *GSLIB : Geostatistical software library and user's guide*,
 997 New York, 1997.

998 Gringarten, E. and Deutsch, C. V.: *Methodology for Variogram Interpretation and Modeling*
 999 *for Improved Reservoir Characterization*, SPE Annual Technical Conference and Exhibition,
 1000 Texas, Houston, 1999.

1001 Gringarten, E. and Deutsch, C. V.: Teacher's Aide Variogram Interpretation and modeling,
 1002 *Mathematical Geology*, 33, 507-534, 2001.

1003 Hanke, J. R., Fischer, M. P., and Pollyea, R. M.: Directional semivariogram analysis to identify
 1004 and rank controls on the spatial variability of fracture networks, *Journal of Structural*
 1005 *Geology*, 108, 34-51, 2018.

1006 Hooker, J. N. and Katz, R. F.: Vein spacing in extending, layered rock: The effect of
 1007 synkinematic cementation, *American Journal of Science*, 315, 32, 2015.

1008 Hooker, J. N., Laubach, S. E., and Marrett, R.: Fracture-aperture size—frequency, spatial
 1009 distribution, and growth processes in strata-bounded and non-strata-bounded fractures,
 1010 Cambrian Mesón Group, NW Argentina, *Journal of Structural Geology*, 54, 54-71, 2013.

1011 Huang, N., Jiang, Y., Liu, R., and Li, B.: Estimation of permeability of 3-D discrete fracture
 1012 networks: An alternative possibility based on trace map analysis, *Engineering Geology*, 226,
 1013 12-19, 2017.

1014 Journel, A. and Zhang, T.: The Necessity of a Multiple-Point Prior Model, *Mathematical*
 1015 *Geology*, 38, 591-610, 2006.

1016 Journel, A. G.: Beyond Covariance: The Advent of Multiple-Point Geostatistics. In:
 1017 *Geostatistics Banff 2004*, Leuangthong, O. and Deutsch, C. V. (Eds.), Springer Netherlands,
 1018 Dordrecht, 2005.

1019 Jung, A., Fenwick, D. H., and Caers, J.: Training image-based scenario modeling of fractured
 1020 reservoirs for flow uncertainty quantification, *Computational Geosciences*, 17, 1015-1031,
 1021 2013.

1022 Karimpouli, S., Tahmasebi, P., Ramandi, H. L., Mostaghimi, P., and Saadatfar, M.: Stochastic
 1023 modeling of coal fracture network by direct use of micro-computed tomography images,
 1024 *International Journal of Coal Geology*, 179, 153-163, 2017.

1025 Kovesi, P.: *MATLAB and Octave Functions for Computer Vision and Image Processing*. 2000.

Lamarche, J., Chabani, A., and Gauthier, B. D. M.: Dimensional threshold for fracture linkage and hooking, *Journal of Structural Geology*, doi: <https://doi.org/10.1016/j.jsg.2017.11.016>, 2017. 2017.

Lamarche, J., Lavenu, A. P. C., Gauthier, B. D. M., Guglielmi, Y., and Jayet, O.: Relationships between fracture patterns, geodynamics and mechanical stratigraphy in Carbonates (South-East Basin, France), *Tectonophysics*, 581, 231–245, 2012.

Laubach, S. E., Lamarche, J., Gauthier, B. D. M., Dunne, W. M., and Sanderson, D. J.: Spatial arrangement of faults and opening-mode fractures, *Journal of Structural Geology*, 108, 2-15, 2018.

Laubach, S. E., Olson, J. E., and Gross, M. R.: Mechanical and fracture stratigraphy, *AAPG Bulletin*, 93, 1413–1426, 2009.

Lavenu, A. P. C., Lamarche, J., Gallois, A., and Gauthier, B. D. M.: Tectonic versus diagenetic origin of fractures in a naturally fractured carbonate reservoir analog (Nerthe anticline, southeastern France), *AAPG Bulletin*, 97, 2207-2232, 2013.

Li, J. Z., Laubach, S. E., Gale, J. F. W., and Marrett, R. A.: Quantifying opening-mode fracture spatial organization in horizontal wellbore image logs, core and outcrop: Application to Upper Cretaceous Frontier Formation tight gas sandstones, USA, *Journal of Structural Geology*, 108, 137-156, 2018.

Liu, X., Srinivasan, S., and Wong, D.: Geological characterization of naturally fractured reservoirs using multiple point geostatistics, 2002.

Liu, X., Zhang, C., Liu, Q., and Birkholzer, J.: Multiple-point statistical prediction on fracture networks at Yucca Mountain, *Environmental Geology*, 57, 1361-1370, 2009.

Lloyd, S. P.: Least Squares Quantization in PCM, *IEEE Transactions on Information Theory*, 28, 9, 1982.

Long, J. C. S. and Witherspoon, P. A.: The relationship of the degree of interconnection to permeability in fracture networks, *Journal of Geophysical Research*, 90, 12, 1985.

Magistrone, C., Meda, M., and Corrao, A.: Faults and fracture network prediction: stress/strain modelling from outcrop analysis to seismic characterisation, Abu Dhabi, UAE, 10-13 November 2014 2014.

Mariethoz, G.: Geological stochastic imaging for aquifer characterization, Doctorate, Faculté des Sciences, Université de Neuchâtel, 229 pp., 2009.

Mariethoz, G., Renard, P., and Straubhaar, J.: The Direct Sampling method to perform multiplepoint geostatistical simulations., *Water Resources research*, 46, 2010.

Marrett, R., Gale, J. F. W., Gómez, L. A., and Laubach, S. E.: Correlation analysis of fracture arrangement in space, *Journal of Structural Geology*, 108, 16-33, 2018.

Mauldon, M., Dunne, W. M., and Rohrbaugh, M. B. J.: Circular scanlines and circular windows: new tools for characterizing the geometry of fracture traces. , *Journal of Structural Geology*, 23, 12, 2001.

Meerschman, E., Pirot, G., Mariethoz, G., Straubhaar, J., Van Meirvenne, M., and Renard, P.: A practical guide to performing multiple-point statistical simulations with the Direct Sampling algorithm, *Computers & Geosciences*, 52, 307-324, 2013.

Montanari, D., Minissale, A., Doveri, M., Gola, G., Trumphy, E., Santilano, A., and Manzella, A.: Geothermal resources within carbonate reservoirs in western Sicily (Italy): A review, *Earth-Science Reviews*, 169, 180-201, 2017.

Olson, J. E., Laubach, S. E., and Lander, R. H.: Natural fracture characterization in tight gas sandstones: Integrating mechanics and diagenesis, *AAPG Bulletin*, 93, 1535-1549, 2009.

1072 Oriani, F., Ohana-Levi, N., Marra, F., Straubhaar, J., Mariethoz, G., Renard, P., Karnieli, A.,
 1073 and Morin, E.: Simulating Small-Scale Rainfall Fields Conditioned by Weather State and
 1074 Elevation: A Data-Driven Approach Based on Rainfall Radar Images, *Water Resources*
 1075 *Research*, 53, 8512-8532, 2017.
 1076 Otsu, N.: A Threshold Selection Method from Gray-Level Histograms, *IEEE Transactions on*
 1077 *Systems, Man, and Cybernetics*, 9, 5, 1979.
 1078 Panza, E., Sessa, E., Agosta, F., and Giorgioni, M.: Discrete Fracture Network modelling of a
 1079 hydrocarbon-bearing, oblique-slip fault zone: Inferences on fault-controlled fluid storage and
 1080 migration properties of carbonate fault damage zones, *Marine and Petroleum Geology*, 89,
 1081 Part 2, 263-279, 2018.
 1082 Reis, Á. F. C., Bezerra, F. H. R., Ferreira, J. M., do Nascimento, A. F., and Lima, C. C.: Stress
 1083 magnitude and orientation in the Potiguar Basin, Brazil: Implications on faulting style and
 1084 reactivation, *Journal of Geophysical Research: Solid Earth*, 118, 5550-5563, 2013.
 1085 Rzonca, B.: Carbonate aquifers with hydraulically non-active matrix: A case study from
 1086 Poland, *Journal of Hydrology*, 355, 202-213, 2008.
 1087 Solano, N., Zambrano, L., and Aguilera, R.: Cumulative Gas Production Distribution on the
 1088 Nikanassin Tight Gas Formation, Alberta and British Columbia, Canada, Trinidad and Tobago
 1089 Energy Resources Conference, Port of Spain, Trinidad, 26, 2010.
 1090 Somasundaram, S., Mund, B., Soni, R., and Sharda, R.: Seismic attribute analysis for fracture
 1091 detection and porosity prediction: A case study from tight volcanic reservoirs, Barmer Basin,
 1092 India, *The Leading Edge*, 36, 7, 2017.
 1093 Straubhaar, J.: Deesse user's guide. The Centre for Hydrogeology and Geothermics (CHYN),
 1094 U. o. N. (Ed.), Neuchâtel, Switzerland, 2017.
 1095 Straubhaar, J., Renard, P., Mariethoz, G., Froidevaux, R., and Besson, O.: An improved
 1096 parallel multiple-point algorithm using a list approach., *Mathematical Geosciences*, 43, 24,
 1097 2011.
 1098 Strebelle, S.: Conditional Simulation of Complex Geological Structures Using Multiple-Point
 1099 Statistics, *Mathematical Geology*, 34, 1-21, 2002.
 1100 Tavani, S., Corradetti, A., and Billi, A.: High precision analysis of an embryonic extensional
 1101 fault-related fold using 3D orthorectified virtual outcrops: The viewpoint importance in
 1102 structural geology, *Journal of Structural Geology*, 86, 200-210, 2016.
 1103 Vollgger, S. A. and Cruden, A. R.: Mapping folds and fractures in basement and cover rocks
 1104 using UAV photogrammetry, Cape Liptrap and Cape Paterson, Victoria, Australia, *Journal of*
 1105 *Structural Geology*, 85, 168-187, 2016.
 1106 Wang, S., Huang, Z., Wu, Y.-S., Winterfeld, P. H., and Zerpa, L. E.: A semi-analytical
 1107 correlation of thermal-hydraulic-mechanical behavior of fractures and its application to
 1108 modeling reservoir scale cold water injection problems in enhanced geothermal reservoirs,
 1109 *Geothermics*, 64, 81-95, 2016.
 1110 Wu, J., Boucher, A., and Zhang, T.: A SGeMS code for pattern simulation of continuous and
 1111 categorical variables: FILTERSIM, *Computers & Geosciences*, 34, 1863-1876, 2008.
 1112 Zhang, L., Kang, Q., Chen, L., Yao, J.: Simulation of flow in multi-scale porous media using the
 1113 lattice boltzmann method on quadtree grids, *Communications in Computational Physics* 19,
 1114 17, 2016.
 1115